

# Measurement of Central Exclusive Production of $h\bar{h}$ pairs $(h=\pi,K,p)$ with Roman Pot detectors in diffractive proton-proton interactions at $\sqrt{s}=200~{\rm GeV}$

Leszek Adamczyk¹, Łukasz Fulek¹, Włodek Guryn², Mariusz Przybycień¹, and Rafał Sikora¹,†

<sup>1</sup>AGH University of Science and Technology, FPACS, Kraków, Poland <sup>2</sup>Brookhaven National Laboratory, Upton, NY, USA <sup>†</sup>e-mail: rafal.sikora@fis.agh.edu.pl

February 7, 2018

#### Abstract

In this note we present analysis of the Central Exclusive Production process using data from proton-proton collisions collected in 2015. This data was collected using the Roman Pot detectors which ensured efficient triggering and measuring diffractively scattered protons. We describe all intermediate stages of analysis involving extraction of the acceptance and efficiency corrections, comparison of data with Monte Carlo models folded into detector response, and study of systematic uncertainties. Finally, we show the physics outcome of the analysis.

# DRAFT

# Contents

_												
	1.1	Central Exclusive Production										
	1.2	Double Pomeron Exchange										
	1.3	Physics motivation for the measurement										
		1.3.1 DIPE differential cross-sections, mass spectrum										
		1.3.2 Absorption effects										
		1.3.3 Size of interaction region										
	ъ.											
<b>2</b>		a set										
	2.1	Trigger										
	2.2	Reconstruction software										
	2.3	Data format										
	2.4	Bad runs										
		2.4.1 RP distance from the beamline										
3	E <sub>vro</sub>	nt selection										
J	3.1	List of cuts										
	$\frac{3.1}{3.2}$											
	3.2	•										
		3.2.1 (C1,C2) Primary vertex and its z-position										
		3.2.2 (C3) TPC tracks										
		3.2.3 (C4) RP tracks										
		3.2.4 (C5) TPC-RP <i>z</i> -vertex matching										
		3.2.5 (C6) BBC-large signal veto										
		3.2.7 (C8) Exclusivity cut (missing $p_T$ cut)										
		3.2.8 (C9) Particle identification										
	3.3	Working point for cuts C6, C7 and C8										
	3.4	Signal per integrated luminosity										
	3.5	Cut flow										
4	<b>C</b>											
4		rections 2										
	4.1	Method of corrections application										
	4.2	Efficiencies and acceptances										
		4.2.1 Trigger efficiency										
		4.2.1.1 Online veto (BBC-small and ZDC veto)										
		4.2.1.2 RP triggering efficiency										
		4.2.1.3 Up and Down RP combination veto										
		4.2.2 Cuts efficiency										
		4.2.2.1 TPC z-vertex cut (C2) $\dots \dots \dots$										
		4.2.2.2 TPC-RP z-vertex matching (C5)										
		4.2.2.3 Primary vertices limit (C1), BBC-large veto (C6) and TOF clusters limit (C7) . 2										
		4.2.2.4 Missing $p_T$ cut (C8)										
		4.2.2.5 Particle identification (C9)										
		4.2.3 RP track acceptance and reconstruction efficiency										
		4.2.4 TPC track acceptance and reconstruction efficiency										
		4.2.5 TOF acceptance, reconstruction and track-matching efficiency										
		4.2.6 TPC vertex reconstruction efficiency										
	4.3	Particle energy loss										
	4.4	Background subtraction										

	4.5	Unfolding	25						
5	6 Backgrounds								
	5.1	Sources of background							
		5.1.1 Non-exclusive background							
	- 0	5.1.2 Exclusive background (particle misidentification)							
	5.2	Background and signal normalization	27						
6	Syst	tematic errors	28						
Lis	List of Figures								
Lis	List of Tables								
Rε	References								

# 1. Introduction

#### 1.1 Central Exclusive Production

The Central Exclusive Production (CEP) takes place when interacting particles form in the mid-rapidity region a state ("central production") whose all constituents/decay products are measured in the detector ("exclusive"). The initial state particles can either dissociate, excite or stay intact. The latter case of CEP in proton-proton collisions can be written as

$$p + p \rightarrow p + X + p \tag{1.1}$$

and depicted as in Fig. 1.1. Mass and rapidity of state X is given by

$$M_X = \sqrt{s(\xi_1 \xi_2 \sin^2(\alpha/2) - (1 - \xi_1 - \xi_2) \cos^2(\alpha/2))} \stackrel{\alpha = \pi}{=} \sqrt{s\xi_1 \xi_2}, \quad (1.2) \qquad y_X = \frac{1}{2} \ln \frac{\xi_1}{\xi_2}, \quad (1.3)$$

where  $\alpha$  is angle between scattered protons and  $\xi = (p_0 - p)/p_0$  is the fractional momentum loss of proton.

# 1.2 Double IPomeron Exchange

Reaction from Eq. (1.1) can exhibit purely electromagnetic  $(\gamma-\gamma)$ , mixed  $(\gamma-\mathcal{O})$  or purely strong nature  $(\mathcal{O}-\mathcal{O})$ . The last type is dominant at RHIC energies. It is characterized by the lack of hard scale (if protons are scattered at small angles), therefore perturbative QCD cannot be applied and Regge theory [1] is used instead. An object  $\mathcal{O}$  does not have unequivocal QCD representation - in Regge formalism it is the so-called "trajectory" (Reggeon,  $\mathbb{R}$ ). Reggeon with quantum numbers of vacuum is called "Pomeron" ( $\mathbb{P}$ ) and  $\mathbb{P}$ - $\mathbb{P}$  reaction (Fig. 1.2) is called "Double Pomeron Exchange".

Processes involing IPomeron exchange are referred as diffraction due to cross-section in scattering angle resembling similar shape to instesity pattern of diffracted light. For low values of Mandelstam t (small scattering angles) cross-section takes exponential form

$$\frac{d\sigma}{d|t|} \propto e^{-B|t|},\tag{1.4}$$

where the slope parameter B reflects the size of target at which  $\mathbb{P}$ omerons scatter.

Diffractive events have specific property of the "rapidity gap" which is an angular region free of hadrons. In DIPE two such gaps are present, marked in Fig. 1.1 as  $\Delta \eta_1$  and  $\Delta \eta_2$ .

DIPE is a spin-parity filter - from the fact that scattered particles have all quantum numbers unchanged after the interaction, central states must satisfy

$$I^G J^{PC} = 0^+ \text{even}^{++}.$$
 (1.5)

The lowest order QCD picture of the IPomeron is a pair of oppositely colored gluons (colour singlet). This fact makes the DIPE recognized as the gluon-rich environment process which should enhance production of the bound states of gluons ("glueballs") or hybrid mesons.

For detailed introduction to the topic of diffraction see Refs. [2,3].

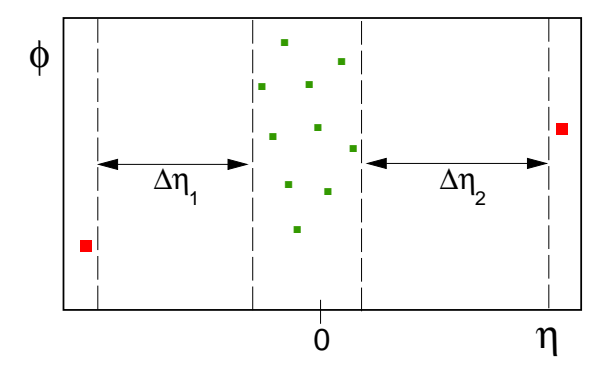


Figure 1.1: Central Exclusive Production in  $\eta$ - $\phi$  space.

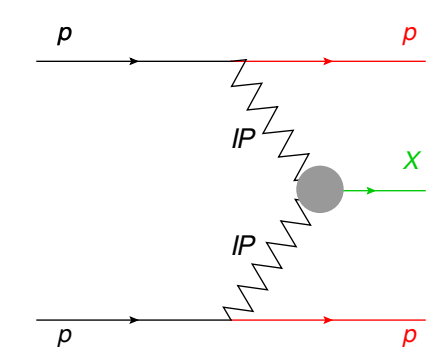


Figure 1.2: Diagram of DIPE process.

# 1.3 Physics motivation for the measurement

STAR collected in 2015 large dataset dedicated for the measurement of the Central Diffraction (DIPE in particular). Since that year the experiment was enriched with Roman Pot Phase II\* subsystem and thus gained possibility of detection of forward protons. It enabled studies of properties of the central state with respect to observables related to exchanged IPomerons. No such measurement was performed before at that high c.m.s. energy ( $\sqrt{s} = 200 \text{ GeV}$ , contamination from IReggeon exchanges is small) which makes it particularly attractive. A list of physics issues that can be covered with the study described in this note is briefly introduced below.

#### 1.3.1 DIPE differential cross-sections, mass spectrum

As stated in Sec. 1.2 DIPE is a soft process whose theoretical description is done mainly using phenomenological tools, thus measurement of differential cross-sections is needed to verify various production models.

The main focus is put on the simplest state (and most numerously) produced in DIPE, namely a pair of oppositely charged pions,  $\pi^+\pi^-$ . It can be formed either in a non-resonant or resonant mechanism. In the first case the  $\pi^+\pi^-$  continuum is formed by the exchange of the off-shell pion between IPomerons. Currently there are two models of this reaction on the market [4,5], [6]. In the second case the IPomerons directly couple into resonance (e.g.  $f_2(1270)$ ), which then decays to  $\pi^+\pi^-$ . Attempts to calculate cross-section for this production mechanism are presented in Ref. [5] and [7].

Understanding of the mass spectrum in  $\pi^+\pi^-$  channel is important to learn about relative contribution from continuum and resonant production, as well as relative production of resonances. Recognition of resonant states may indicate candidates for low-mass glueballs of  $J^{PC}=0^{++}$ , however presence of underlaying scalar  $q\bar{q}$  states makes this task challenging.

Other channels, like  $K^+K^-$ , are also of great interest. Comparison of the cross-sections for production of  $\pi^+\pi^-$  and  $K^+K^-$  gives information about strength of the Pomeron coupling to different quark flavors. Also, structures in  $d\sigma/dm$  can be easier attributed to resonances by measuring more than one channel and known branching ratios thereof.

Detection of intact protons scattered at very small angle with respect to the beamline enables determination of the reaction plane which makes the Partial Wave Analysis (PWA) possible. It also allows to look at the the cross-sections more differentially, especially with respect to properties of exchanged Pomerons, like carried squared four-momentum t, azimuthal separation of Pomerons in the transverse plane  $\Delta \varphi$  or relative momentum of Pomerons  $\Delta p_T$ . The last quantity was proposed to distinguish pure  $q\bar{q}$  states from these with gluonic content [8].

#### 1.3.2 Absorption effects

One can imagine in diagram in Fig. 1.2 additional soft lines e.g. between protons in the initial state or one of Pomerons and final state proton. These so-called rescattering effects (or absorption effects) lead to production of hadrons other than these belonging to central state X hence the diffractive signature of an event in form of rapidity gap is no longer present. Measurement of the probability that the state X will remain exclusive and forward protons will remain intact, in other words the rapidity gap survival probability  $S^2$ , would be valuable ingredient for development of absorption models.

## 1.3.3 Size of interaction region

From the measurement of protons in Roman Pots one is able to reconstruct squared four-momenta transferred in proton-Pomeron vertices and determine the differential cross-section  $d\sigma/d|t|$ . Fit of exponent allows to extract the slope parameter B, which may depend on the Pomeron-Pomeron c.m.s. energy, or in other words on the mass of diffractive system X. Knowledge on the slope parameter gives insight to the volume and distribution of Pomerons inside proton.

# 2. Data set

# 2.1 Trigger

The main trigger designed for studies of Central Diffraction in run 15 was RP\_CPT2. It was formed of the following conditions combined by logical AND (&&):

- 1. (ET && !IT) || (!ET && IT) = signal in at least one RP on each side of the STAR central detector to ensure presence of two forward-scattered protons; a veto was imposed on simultaneous signal in RPs above and below the beamline, which might have originated either from proton dissociation, or pile-up event, or beam halo proton etc.,
- 2. !BBCE && !BBCW && !ZDCE && !ZDCW = veto on any signal in small BBC tiles or ZDCs on any side of STAR central detector such requirement is in accordance with the double-gap topology of CEP events, it mostly filtered out CEP events with parallel pile-up event(s),
- 3.  $TOF \ge 2$  = at least 2 hits in TOF aim of this condition was to ensure activity in the mid-rapidity; since the lowest multiplicity allowed in CEP is 2, that was the lower threshold of L0 TOF multiplicity.

This trigger was running with an average prescale of 5 and average DAQ rate of 250 Hz, which allowed to collect in total about 560 M events corresponding to 16.5 pb<sup>-1</sup> of integrated luminosity. More information about number of events per run, rates etc. can be found under link provided in Ref. [9], which contains selected data from STAR run log [10]. Luminosity data used in this analysis comes from Ref. [11].

All RP triggers which were intended for usage in diffractive physics analyses or efficiency studies are listed in Tab. 2.1. Components used in definitions of these triggers are outlined in Fig. 2.1. Detailed explanation of all trigger bits can be found in Refs. [12,13]. Explanation of naming convention in Roman Pot system can be found in Ref. [14].

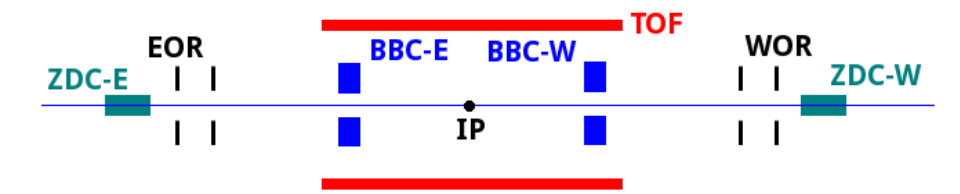


Figure 2.1: Sketch of the trigger components used in definitions of diffractive triggers in run 15.

${f Trigger} \ {f name}$	Definition	Events [M]	Comment
RP_CP	EOR && WOR	73.3	Loose trigger (mostly elastic events) designed for monitoring/trigger efficiency study
RP_CPT	EOR && WOR && !BBCE && !BBCW && !ZDCE && !ZDCW && TOF≥1	38.9	Intended to be main CEP trigger (later switched to RP_CPT2 due to large prescale)
RP_CPT2	(ET && !IT)    (!ET && IT) && !BBCE && !BBCW && !ZDCE && !ZDCW && TOF≥2	556.5	Main CEP trigger Note: On Apr 14 added upper TOF limit (10)
RP_CPX	IT && !BBCE && !BBCW && !ZDCE && !ZDCW && TOF≥2	40.1	The same as RP_CPT2 but only IT configuration
RP_CPEI	ET && IT && !BBCE && !BBCW && !ZDCE && !ZDCW && TOF>2	15.6	Control trigger for CPT2 to estimate effect of !(ET && IT) veto

Table 2.1: Central Diffraction physics triggers and control triggers involving Roman Pot detectors in run 15.

## 2.2 Reconstruction software

Raw data was processed with STAR libraries in versions SL15f. All four trigger datasets were processed: production\_pp200trans\_2015, production\_pp200long2\_2015, production\_pp200long3\_2015 and production\_pp200long\_2015 (see [15]).

The following BFC options were used in the reconstruction:

DbV20160418,pp2015c,btof,mtd,mtdCalib,pp2pp,-beamline,beamline3D,useBTOFmatchOnly,VFStoreX,fmsDat,fmsPoint,fpsDat,BEmcChkStat,-evout,CorrX,OSpaceZ2,OGridLeak3D,-hitfilt

Main attention should be put on option **useBTOFmatchOnly** which forced vertexing algorithm to form vertices only from the global TPC tracks which are matched with hits in the TOF system. This solution was found to yield significantly larger signal reconstruction efficiency (vertexing efficiency) and better resolutions. The study which lead to above conclusions, presented in Ref. [16], was performed on the same dataset processed with older libraries SL15k (without useBTOFmatchOnly option).

## 2.3 Data format

The analyzed data was stored in ROOT files in the picoDST format which was in large part a skimmed MuDST (standard STAR format). The picoDST format was introduced in Ref. [17]. PicoDST description files (C++ headers etc.) can be found in the analysis code repository [18].

#### 2.4 Bad runs

Analysis of CEP was performed on the data from runs with completion status "Successful" in the STAR run log. However, based on additional requirements explained below, some runs were omitted from analysis.

#### 2.4.1 RP distance from the beamline

 $16065025\ 16065026\ 16065026\ 16065028\ 16072057\ 16072058\ 16077055\ 16083006\ 16083007\ 16106031$ 

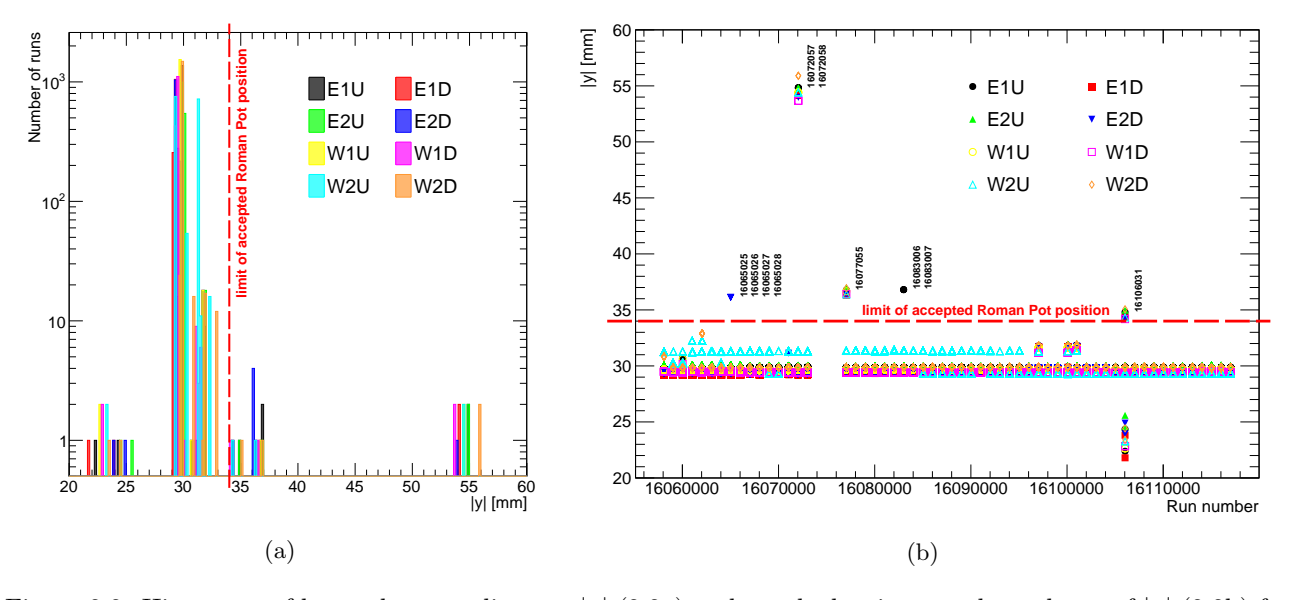


Figure 2.2: Histogram of beam-detector distance |y| (2.2a) and graph showing run-dependence of |y| (2.2b) for all Roman Pots.

# 3. Event selection

Complete list of analysis cuts used for signal extraction is presented in Sec. 3.1. Detailed description of each cut can be found in Sec. 3.2.

# 3.1 List of $cuts^1$

- C1. Exactly 1 primary vertex with TPC track(s) matched with hits in TOF.
- C2. TPC vertex from C1 is placed within  $|z_{vx}| < 100$  cm.
- C3. Exactly 2 opposite-sign primary TPC tracks (C3.2) of good quality (C3.4) matched with hits in TOF (C3.1), reconstructed within region of high TPC acceptance (C3.3) and with small distance of closest approach (DCA) to the vertex (C3.5).
  - C3.1. Exactly 2 TOF-matched (match flag > 0) primary tracks,
  - C3.2. Tracks are of opposite signs,
  - C3.3. Both tracks are contained within the kinematic range:

$$|\eta| < 1$$
,  $p_T > 0.2 \text{ GeV}/c$ ,

C3.4. Both tracks satisfy quality criteria:

$$N_{\rm hits}^{\rm fit} \geq 25, \quad N_{\rm hits}^{\rm dE/dx} \geq 15, \quad N_{\rm hits}^{\rm fit}/N_{\rm hits}^{\rm poss} \geq 0.52, \quad |d_0| < 2~{\rm cm}, \quad |z_0| < 200~{\rm cm},$$

C3.5. Both tracks match well to the primary vertex (DCA is small):

$$DCA(R) < 1.5 \text{ cm}, \quad DCA(z) < 1 \text{ cm}.$$

- C4. Exactly 1 RP track on each side of STAR central detector (C4.3) of good quality (C4.1), with local angles consistent with the IP being the track origin (C4.2), lying within fiducial region of high geometrical acceptance (C4.4).
  - C4.1. RP tracks contain only track-points with at least 3 (out of 4) planes used in reconstrucion,
  - C4.2. Local angles [mrad] lie within  $-1.2 < \theta_x^{\text{RP}} < 5.0$  and  $1.5 < |\theta_y^{\text{RP}}| < 4.5$ ,
  - C4.3. Exactly 1 track passing cuts C4.1-C4.2 per side,
  - **C4.4.** Tracks passing cut C4.3 lie within the  $(p_x, p_y)$  region defined as:  $|p_y| > 0.2 \text{ GeV}/c$ ,  $(p_x/(\text{GeV}/c) + 0.3)^2 + (p_y/(\text{GeV}/c))^2 < 0.46^2$ ,  $(p_x/(\text{GeV}/c) 0.15)^2 + (p_y/(\text{GeV}/c))^2 < 0.42^2$ .
- C5. Vertex z-positions measured in TPC and reconstructed from the difference of proton detection time in west and east RPs are consistent with each other within the resolution:  $|z_{\text{vx}}^{\text{TPC}} z_{\text{vx}}^{\text{RP}}| < 36 \text{ cm}$ .
- C6. No signal in any tile of BBC-large (east or west) with ADC > 40 and 100 < TDC < 2400.
- C7. Maximally 2 reconstructed TOF clusters  $N_{\rm clstrs}^{\rm TOF} \leq 2$ .
- C8. Missing (total) momentum of TPC tracks and RP tracks  $p_T^{\text{miss}} < 75 \text{ MeV}/c$ .
- C9. Particle (pair) identification:

# 3.2 Description of cuts

# 3.2.1 (C1,C2) Primary vertex and its z-position

<sup>&</sup>lt;sup>1</sup>Some cuts (e.g. C3) are decomposed to constituent sub-cuts. Cut is formed by the logical AND of all its sub-cuts.

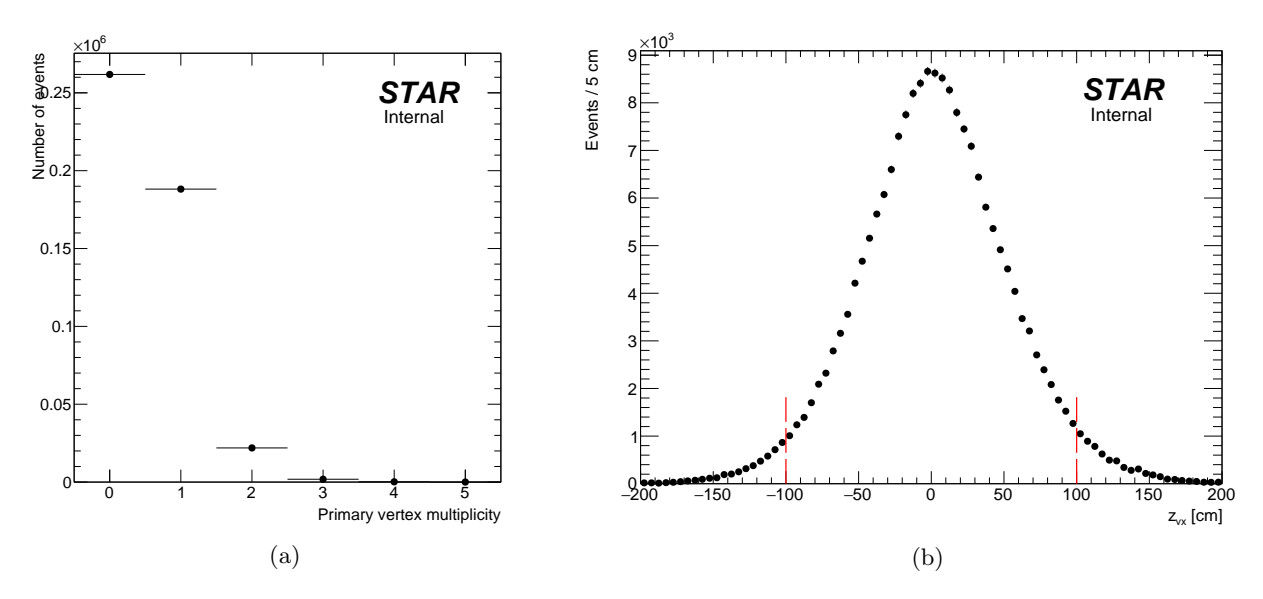
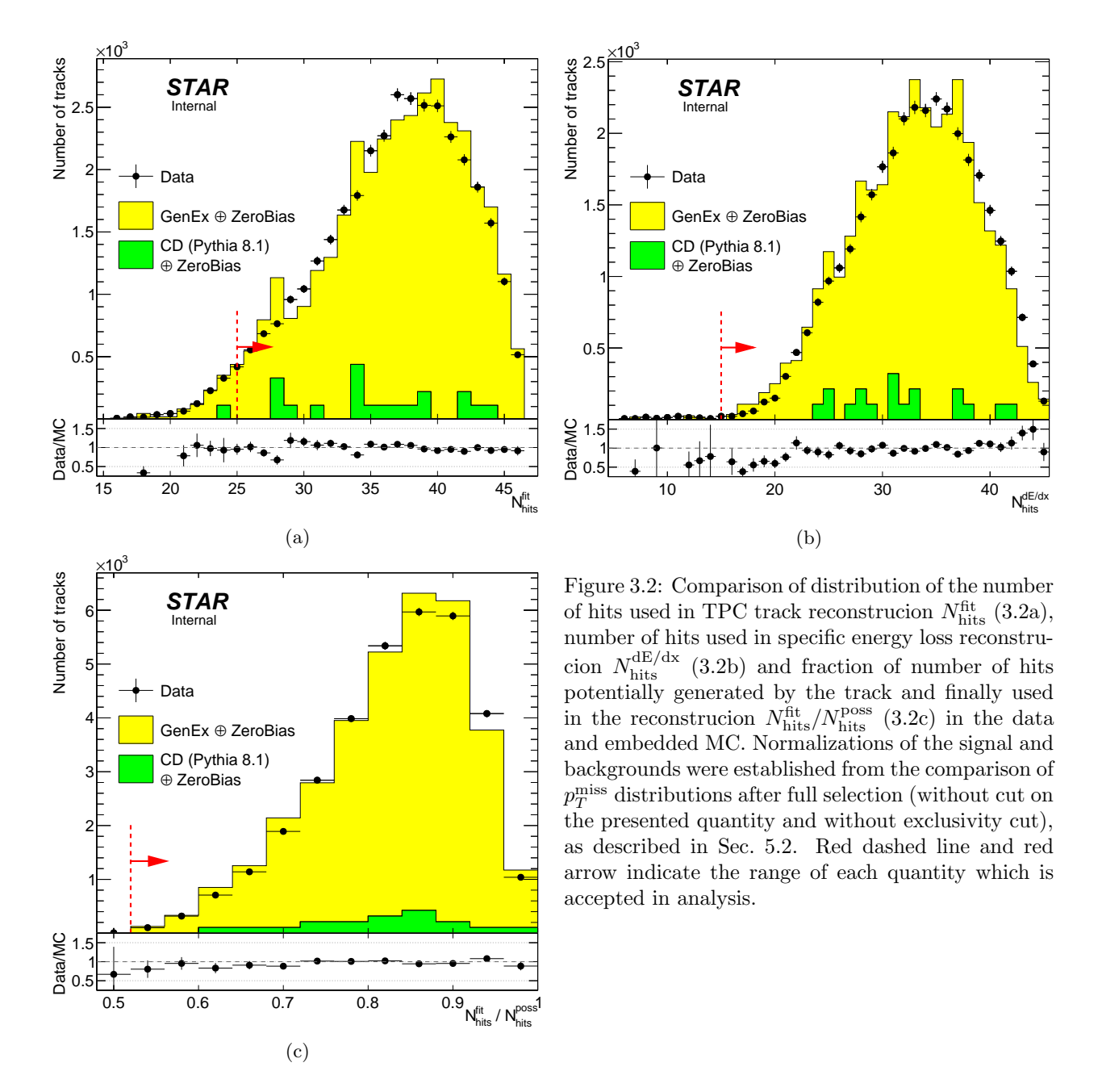


Figure 3.1: Primary vertex multiplicty (Fig. 3.1a) and z-position of the single primary vertex (Fig. 3.1b).

# 3.2.2 (C3) TPC tracks



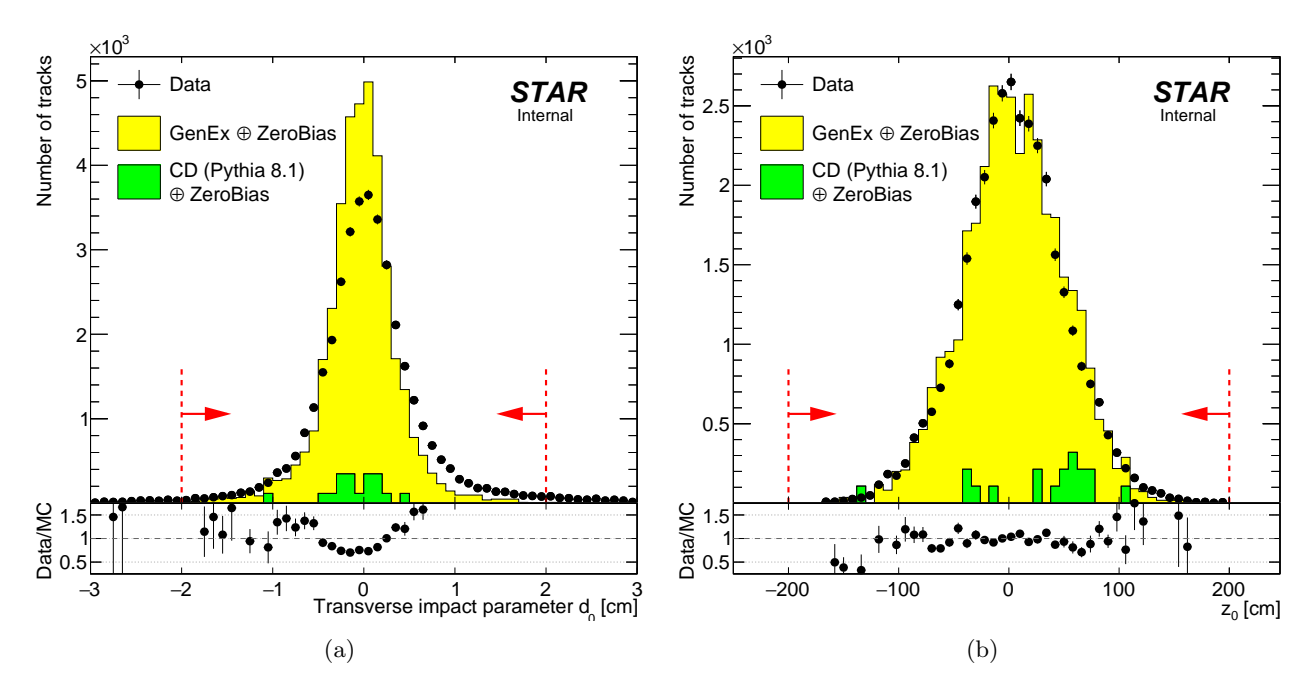


Figure 3.3: Comparison of distribution of the transverse impact parameter  $d_0$  (3.3a) and the longitudinal impact parameter  $z_0$  (3.3b) in the data and embedded MC. Normalizations of the signal and backgrounds were established from the comparison of  $p_T^{\text{miss}}$  distributions after full selection (without cut on the presented quantity and without exclusivity cut), as described in Sec. 5.2. Red dashed lines and red arrows indicate the range of each quantity which is accepted in analysis.

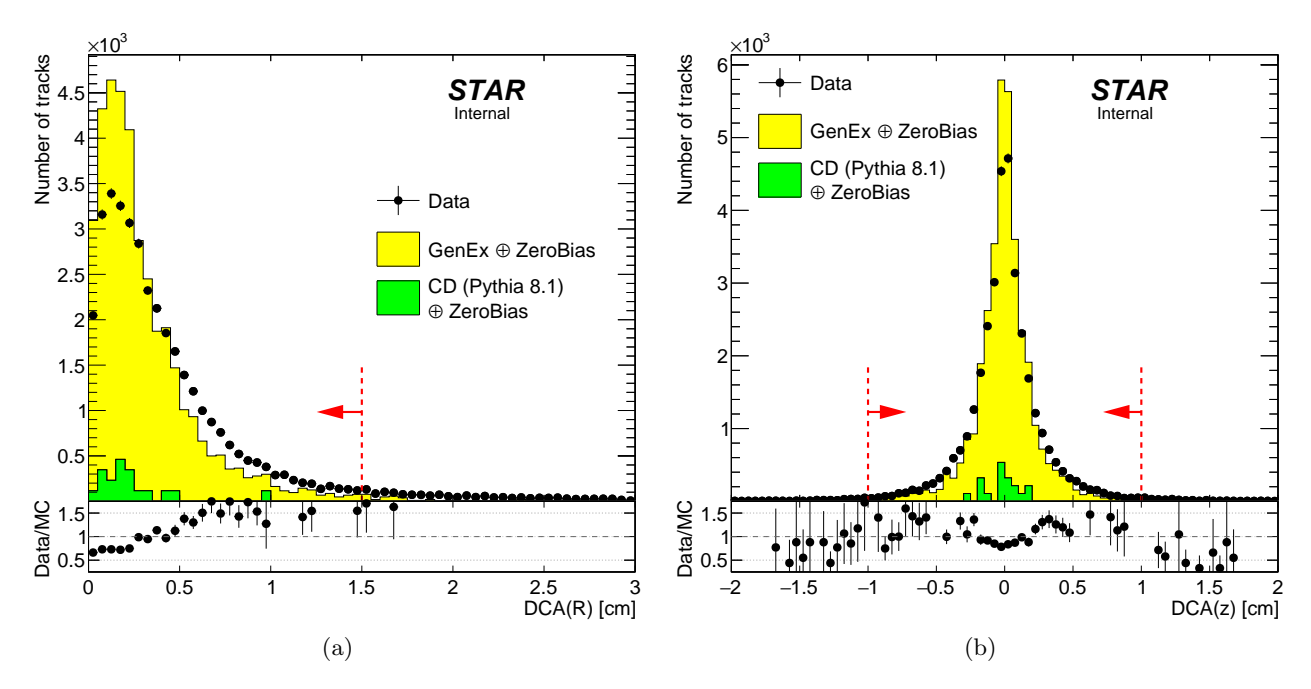


Figure 3.4: Comparison of distribution of the distance of closest approach of the track to the vertex in the xy-plane DCA(R) (3.4a) and the the distance of closest approach of the track to the vertex along the z-axis DCA(z) (3.4b) in the data and embedded MC. Normalizations of the signal and backgrounds were established from the comparison of  $p_T^{\text{miss}}$  distributions after full selection (without cut on the presented quantity and without exclusivity cut), as described in Sec. 5.2. Red dashed lines and red arrows indicate the range of each quantity which is accepted in analysis.

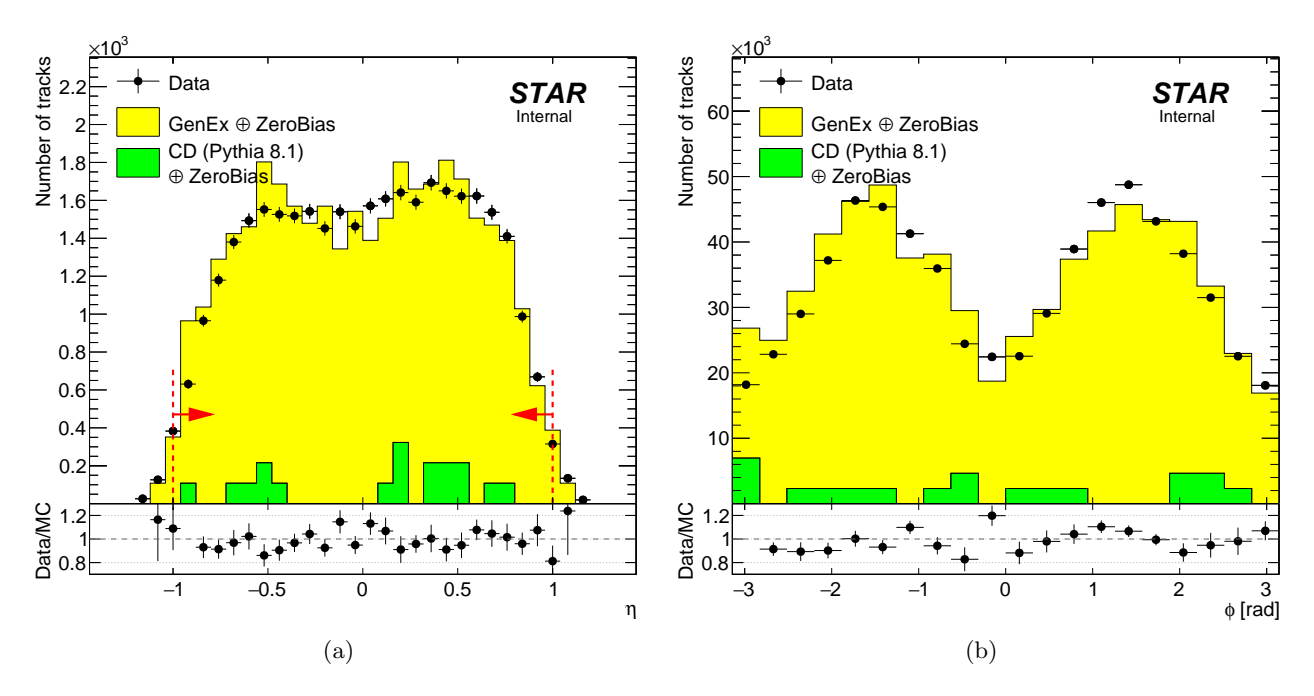


Figure 3.5: Comparison of the track pseudorapidity  $\eta$  (3.5a) and the track azimuthal angle  $\phi$  (3.5b) in the data and embedded MC. Normalizations of the signal and backgrounds were established from the comparison of  $p_T^{\rm miss}$  distributions after full selection (without cut on the presented quantity and without exclusivity cut), as described in Sec. 5.2. Red dashed lines and red arrows indicate the range of each quantity which is accepted in analysis.

# 3.2.3 (C4) RP tracks

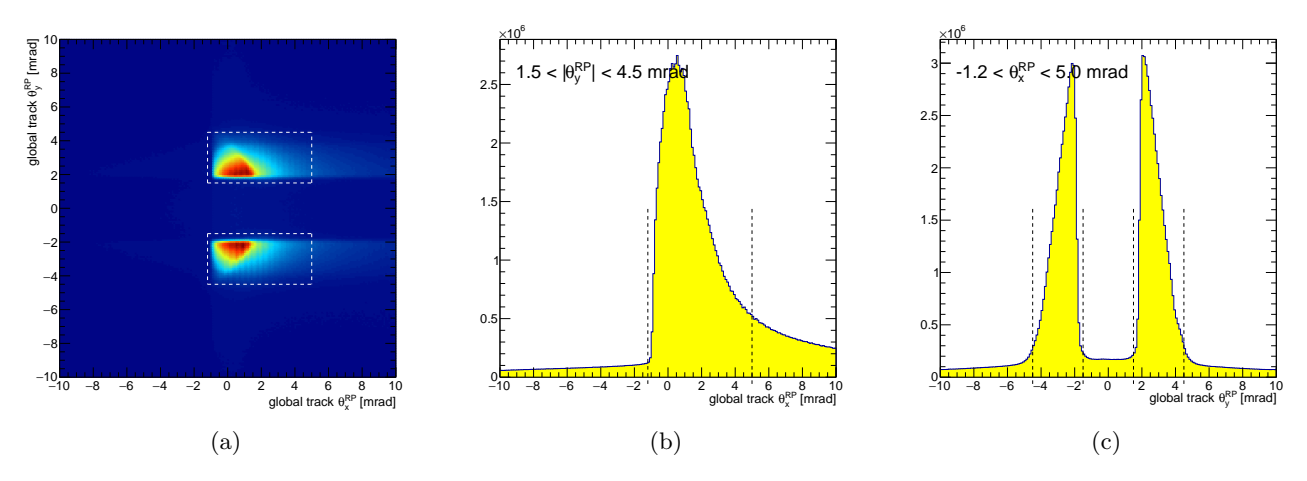


Figure 3.6: Local angles of global tracks in Roman Pots.

# 3.2.4 (C5) TPC-RP z-vertex matching

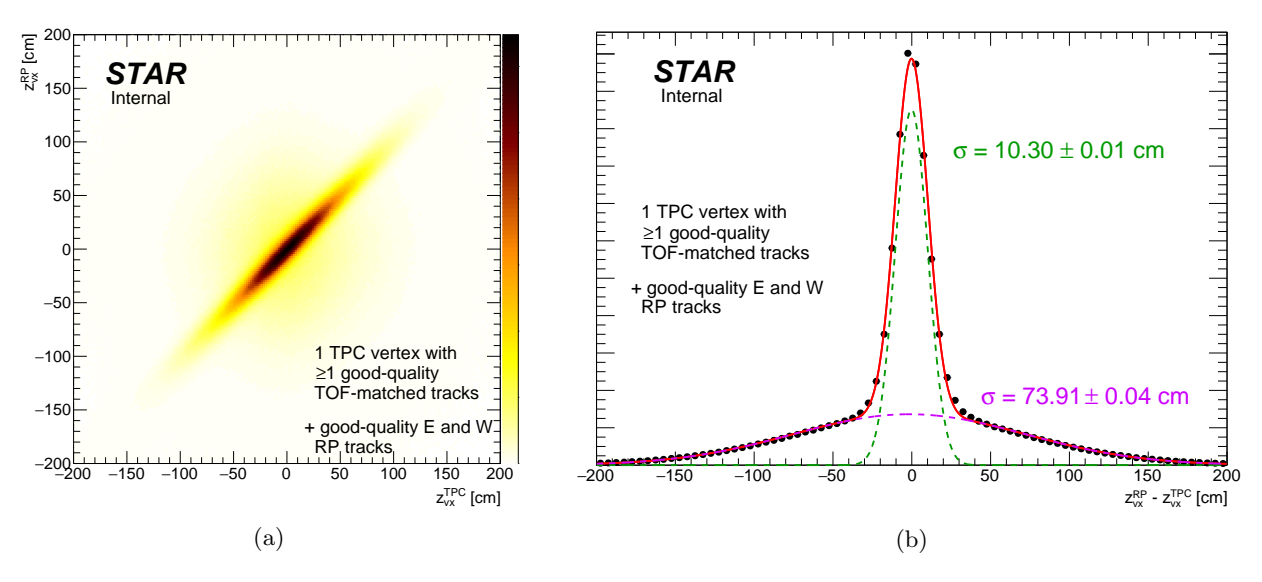


Figure 3.7: Correlation (Fig. 3.7a) and difference (Fig. 3.7b) of z-vertex position measured in Roman Pots and TPC.

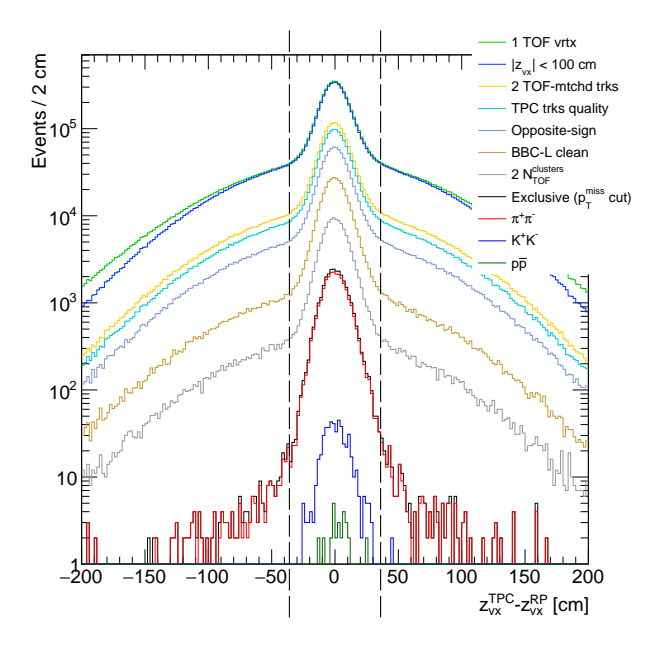
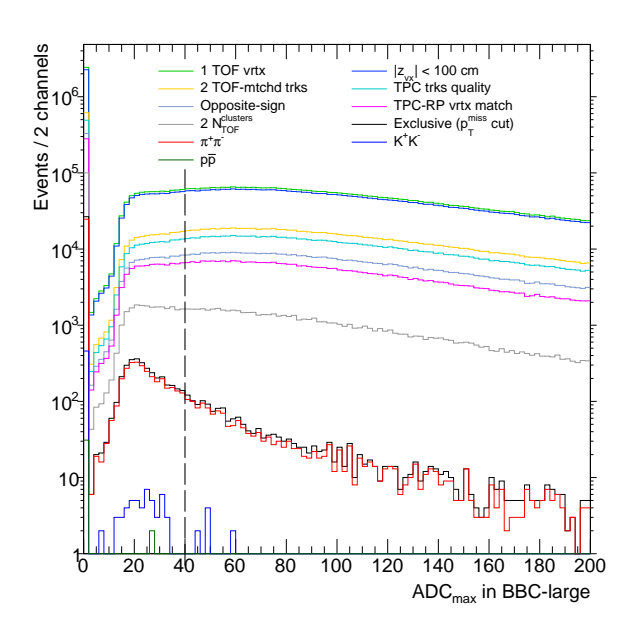


Figure 3.8: Delta z-vx.

# 3.2.5 (C6) BBC-large signal veto



Figure~3.9:~MaxAdcBbcLarge.

# 3.2.6 (C7) TOF clusters limit

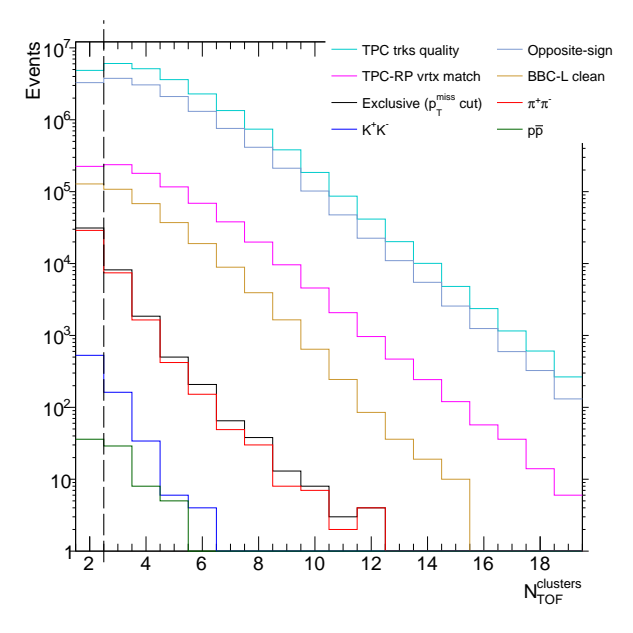


Figure 3.10: NTofClusters.

# 3.2.7 (C8) Exclusivity cut (missing $p_T$ cut)

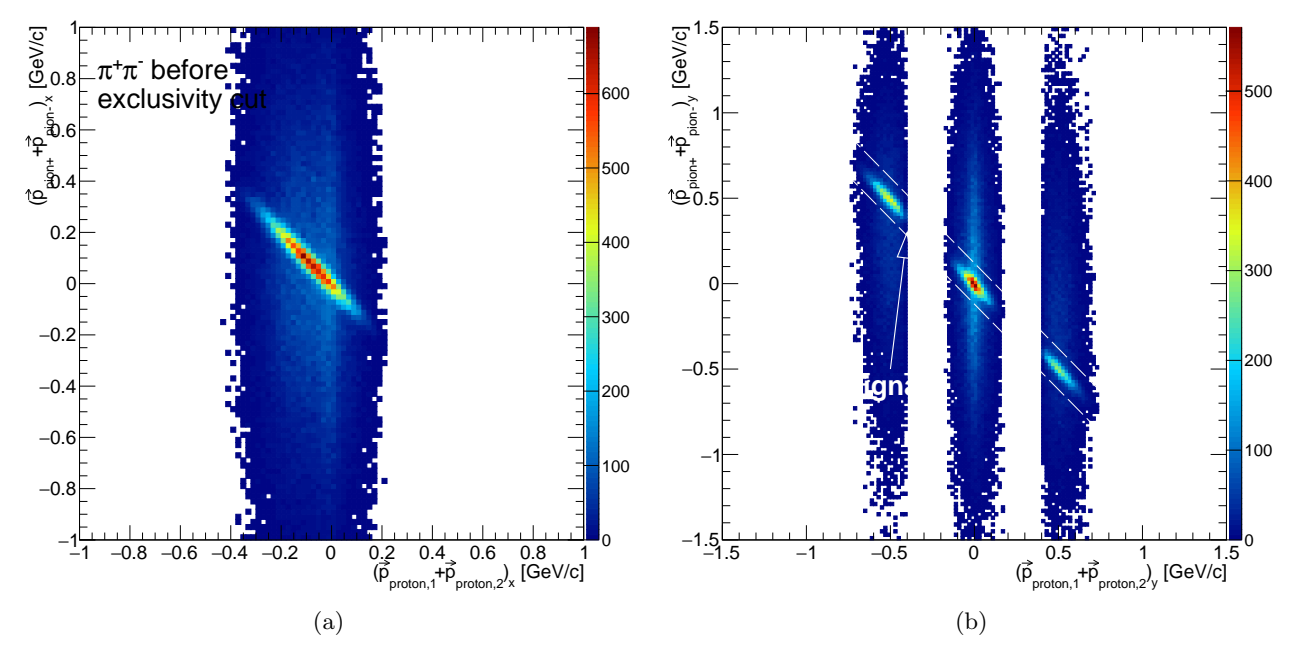


Figure 3.11: Correlation between sum of corresponding momentum components (x in Fig. 3.11a and y in Fig. 3.11b) of Roman Pot proton tracks and TPC tracks.

Tutaj dodac rysunki z suma 1D tych wielkosci i uzasadnic stosowanie ciecia na missing pT takimi samymi rozdzielczosciami w x i y

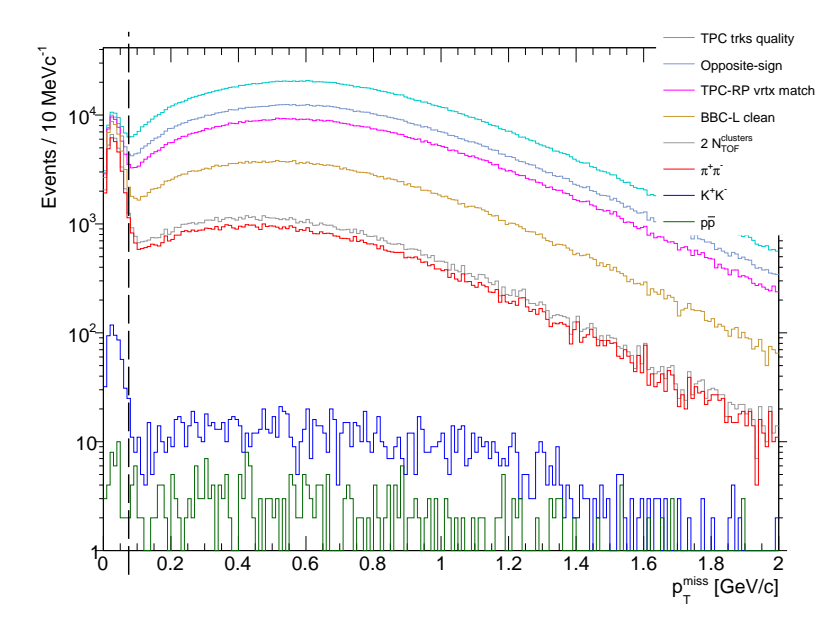


Figure 3.12: MissingPt.

# 3.2.8 (C9) Particle identification

In addition to information from the TPC we use time of hit detection in the barrel TOF subsystem. From the simple algebra describing relation between track lengths, momenta and times of hit detection one can derive formula for the squared mass of two particles, assuming that their masses are equal (particles are of the same type):

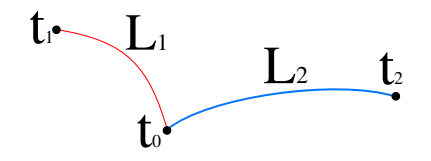


Figure 3.13: Scheme of two central tracks of lengths  $L_1$  and  $L_2$ , produced in common vertex in moment  $t_0$ , hitting cells in TOF detector in moments  $t_1$  and  $t_2$ .

$$\begin{cases}
t_1 - t_0 = L_1 \sqrt{1 + \frac{m_1^2}{p_1^2}}, \\
t_2 - t_0 = L_2 \sqrt{1 + \frac{m_2^2}{p_2^2}},
\end{cases}$$
(3.1)

$$\Delta t = t_1 - t_2 = L_1 \sqrt{1 + \frac{m_1^2}{p_1^2}} - L_2 \sqrt{1 + \frac{m_2^2}{p_2^2}}.$$
 (3.2)

Assuming  $m_1 = m_2 = m \rightarrow m^2$  from quadratic eq.

Parameters of the quadratic equation whose solution is suqared mass and the final formula for  $m_{\text{TOF}}^2$  are given below:

$$\mathcal{A} = -2\frac{L_1^2 L_2^2}{p_1^2 p_2^2} + \frac{L_1^4}{p_1^4} + \frac{L_2^4}{p_2^4},\tag{3.3}$$

$$\mathcal{B} = -2L_1^2 L_2^2 \left( \frac{1}{p_1^2} + \frac{1}{p_2^2} \right) + \frac{2L_1^4}{p_1^2} + \frac{2L_2^4}{p_2^2} - 2\left(\Delta t\right)^2 \left( \frac{L_1^2}{p_1^2} + \frac{L_2^2}{p_2^2} \right),\tag{3.4}$$

$$C = (\Delta t)^4 - 2(\Delta t)^2 (L_1^2 + L_2^2) + L_1^4 + L_2^4 - 2L_1^2 L_2^2,$$
(3.5)

$$m_{\text{\tiny TOF}}^2 = \frac{-\mathcal{B} + \sqrt{\mathcal{B}^2 - 4\mathcal{A}\mathcal{C}}}{2\mathcal{A}}.$$
 (3.6)

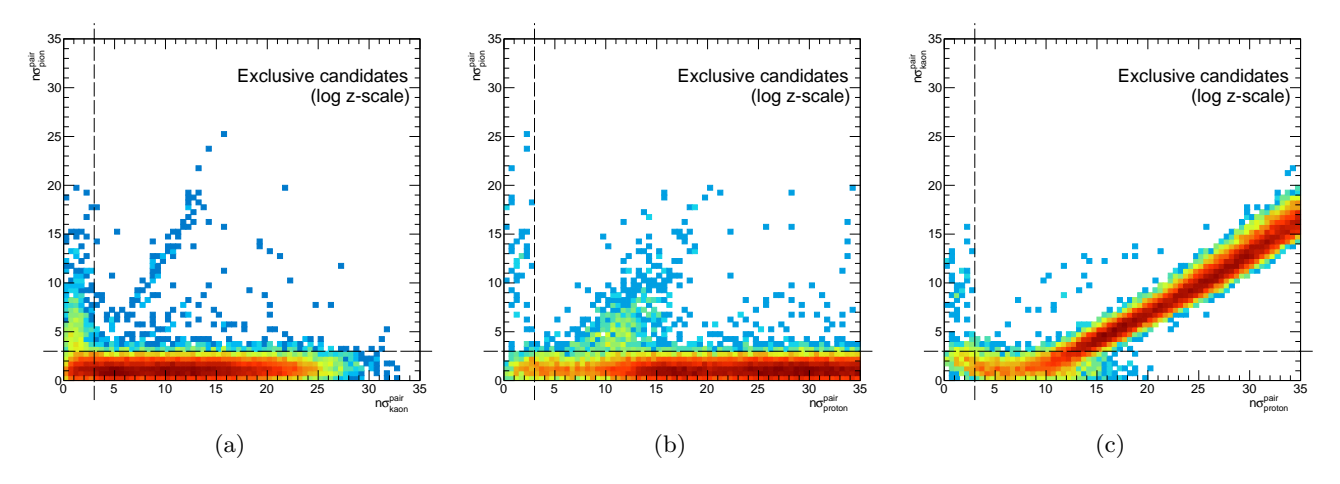


Figure 3.14: Correlation between  $n\sigma^{\text{pair}}$  from TPC for  $\pi^+\pi^-$ ,  $K^+K^-$  and  $p\bar{p}$ .

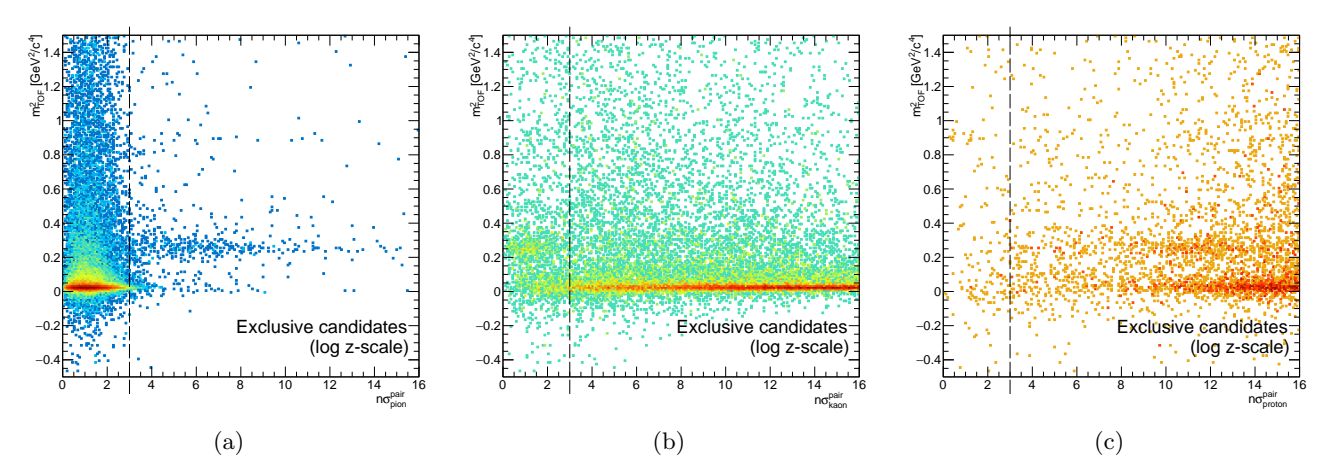


Figure 3.15: Correlation between  $m^2$  from TOF and  $n\sigma^{\text{pair}}$  from TPC for  $\pi^+\pi^-$ ,  $K^+K^-$  and  $p\bar{p}$ .

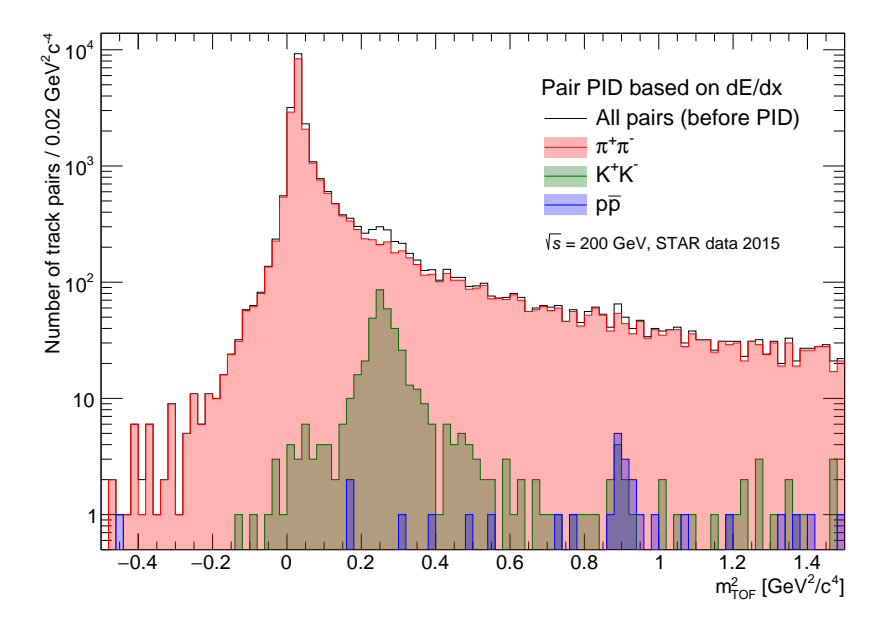
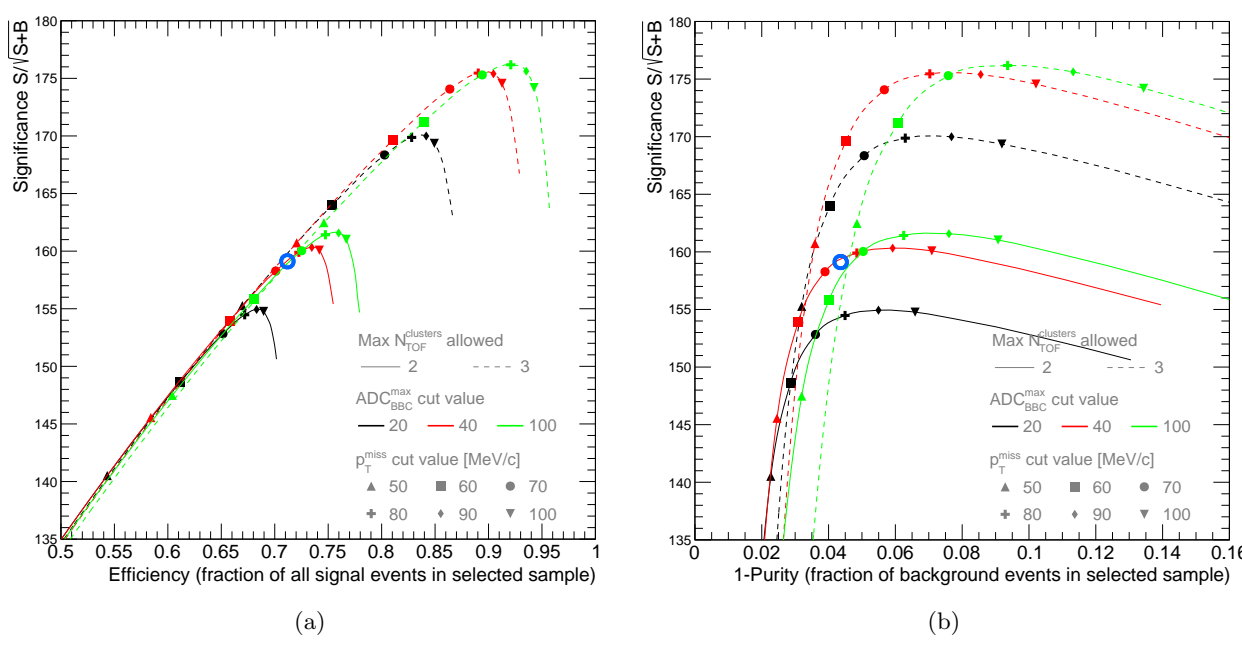


Figure 3.16: Squared particle mass from TOF for candidates of given PID selected based on dE/dx in TPC.

# 3.3 Working point for cuts C6, C7 and C8

$$\text{Significance} = \frac{N_{\text{signal}}^{\text{cut}}}{\sqrt{N_{\text{signal}}^{\text{cut}} + N_{\text{bkgd}}^{\text{cut}}}}, \quad (3.7) \quad \text{Efficiency} = \frac{N_{\text{signal}}^{\text{cut}}}{N_{\text{signal}}^{\text{no cut}}}, \quad (3.8) \quad \text{Purity} = \frac{N_{\text{signal}}^{\text{cut}}}{N_{\text{signal}}^{\text{cut}} + N_{\text{bkgd}}^{\text{cut}}}, \quad (3.9) \quad \text{Purity} = \frac{N_{\text{signal}}^{\text{cut}}}{N_{\text{signal}}^{\text{cut}} + N_{\text{bkgd}}^{\text{cut}}},$$



Efficiency (fragtion of all signal events ig selected sample) 2: 0.0 9: 0.0 5: 0.0 9: cut value 40 - 20 cut value [MeV/c] **6**0 50 . 80 90 0.04 0.06 0.08 0.1 0.12 0.14 1-Purity (fraction of background events in selected sample) (c)

Figure 3.17: Relation between  $\pi^+\pi^-$  signal significance and efficiency (3.17a), significance and purity (3.17b), and efficiency and purity (3.17c) as a function of cut thresholds in BBC-large veto (C6), TOF cluster limit (C7) and exclusivity cut (C8). Lines show forementioned relations with changing  $p_T^{\rm miss}$  cut whose some specific values are indicated with different markers. Color denotes ADC threshold in BBC-large veto (black, red or green). Style of line (solid or dashed) denotes  $N_{\rm clstrs}^{\rm TOF}$  limit. Working point considered optimal is marked with opened blue circle.

# 3.4 Signal per integrated luminosity

# 3.5 Cut flow

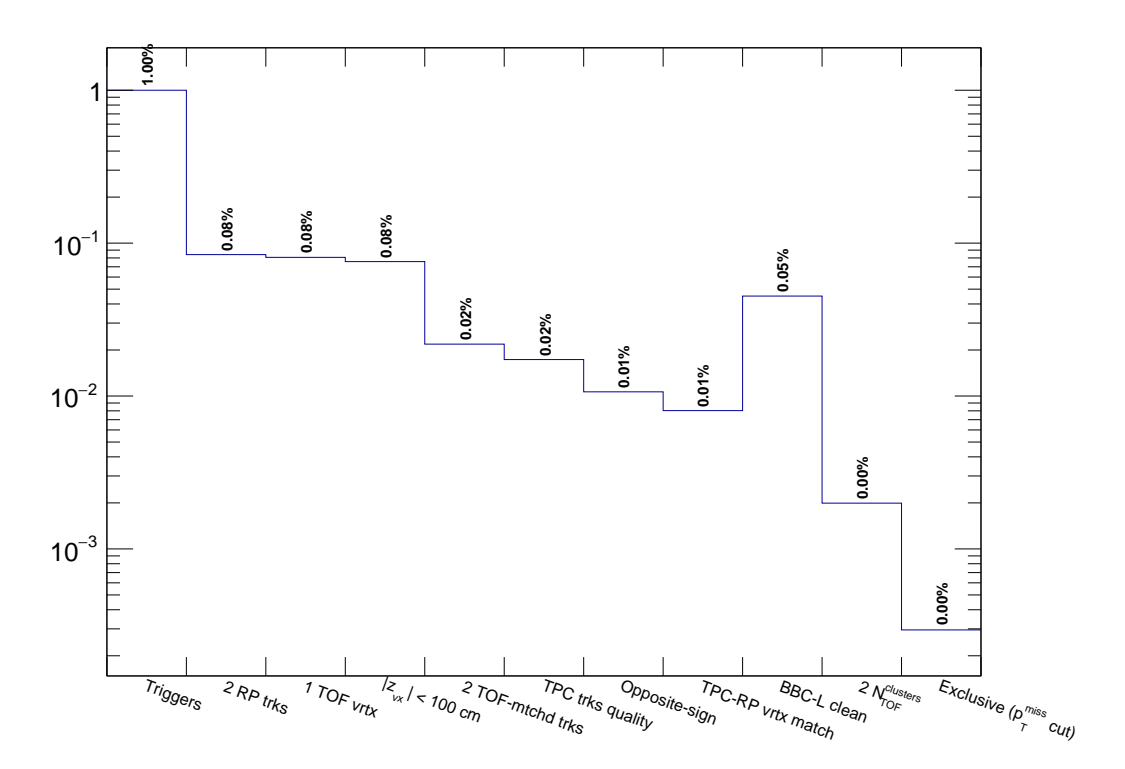


Figure 3.18: Cut flow.

# 4. Corrections

# 4.1 Method of corrections application

$$\frac{d\sigma}{dq} = \frac{1}{\Delta q} \times \frac{1}{\varepsilon} \times \frac{N^w - N_{\text{bkgd}}^w}{L_{\text{int}}^{\text{eff}}}$$
(4.1)

$$L_{\rm int}^{\rm eff} = \sum_{\rm run} L_{\rm int}^{\rm run} \times \epsilon_{\rm veto}(L^{\rm run})$$
(4.2)

$$\varepsilon = \epsilon_{\text{ET/IT}} \times \epsilon_{\text{vrtx}}(q) \times \epsilon_{C2} \times \epsilon_{C5} \times \epsilon_{C8} \times \epsilon_{\text{PID}}(q)$$
(4.3)

$$N^w = \sum_{\text{event}} w_{\text{event}} \tag{4.4}$$

$$w = \left[ \prod_{\text{sign}} \epsilon_{\text{TOF}}(\text{sign}, \text{PID}, p_T, z_{vx}, \eta) \times \prod_{\text{sign}} \epsilon_{\text{TPC}}(\text{sign}, \text{PID}, p_T, z_{vx}, \eta) \times \prod_{\text{side}} \epsilon_{\text{RP}}^{\text{side}}(p_x, p_y) \right]^{-1},$$

$$\text{sign} \in \{+, -\}, \text{ side} \in \{E, W\}$$

$$(4.5)$$

# 4.2 Efficiencies and acceptances

#### 4.2.1 Trigger efficiency

#### 4.2.1.1 Online veto (BBC-small and ZDC veto)

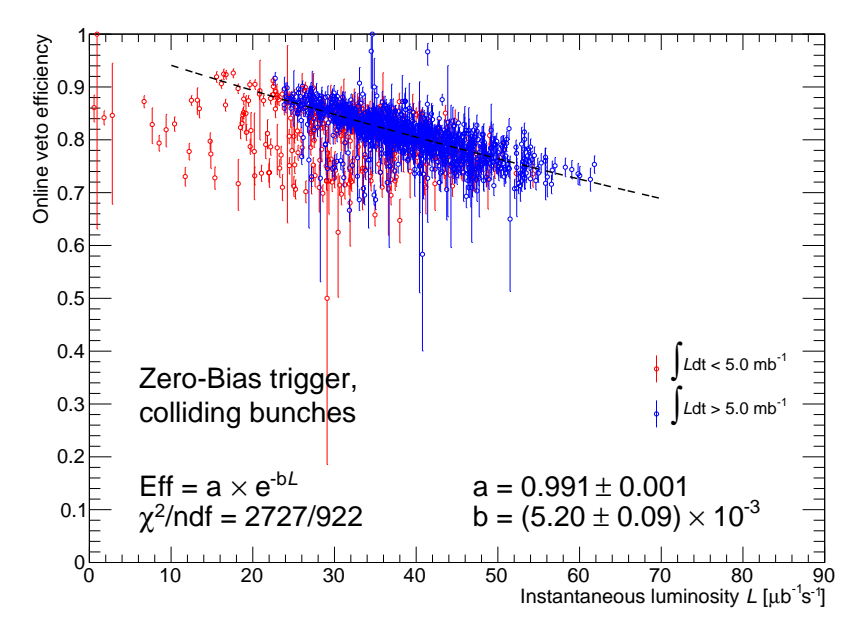


Figure 4.1: Overall efficiency of the online BBC-small and ZDC veto as a function of instantaneous luminosity.

- 4.2.1.2 RP triggering efficiency
- 4.2.1.3 Up and Down RP combination veto
- 4.2.2 Cuts efficiency
- 4.2.2.1 TPC z-vertex cut (C2)
- 4.2.2.2 TPC-RP z-vertex matching (C5)
- 4.2.2.3 Primary vertices limit (C1), BBC-large veto (C6) and TOF clusters limit (C7)

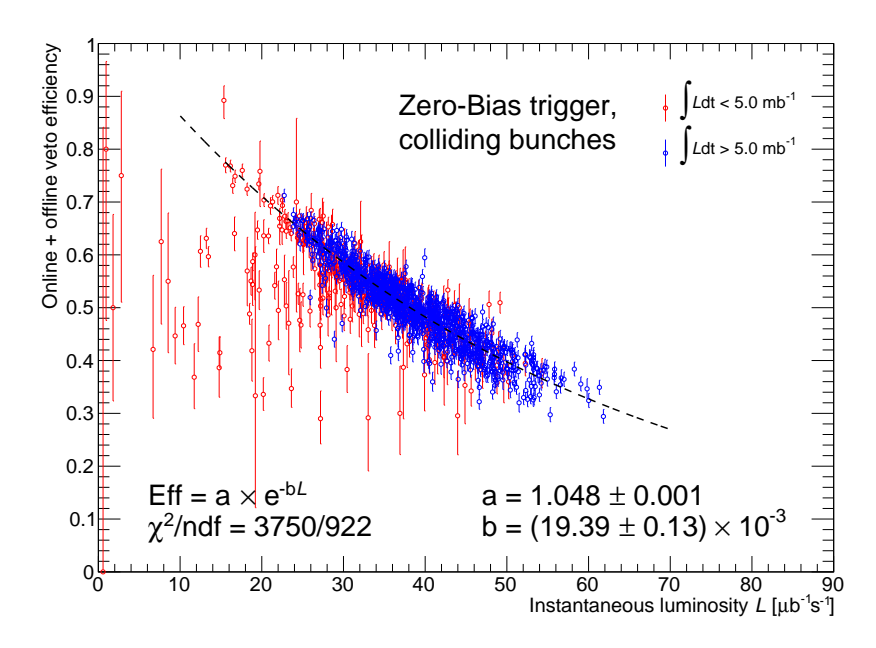


Figure 4.2: Overall efficiency of the online BBC-small and ZDC veto, primary vertices limit (C1), BBC-large veto (C6) and TOF clusters limit (C7) as a function of instantaneous luminosity.

#### 4.2.2.4 Missing $p_T$ cut (C8)

#### 4.2.2.5 Particle identification (C9)

It is possible to transform dE/dx in MC to make it follow the shape of dE/dx in the data. We know that nSigmaX (where X=Pion, Kaon, Proton, ...) variable follows a gaussian distribution (for particle X)

$$nSigmaX = \left(\ln \frac{dE/dx}{\langle dE/dx \rangle_X}\right) / \sigma_{dE/dx}, \qquad f(nSigmaX) = \mathcal{N}(nSigmaX; \mu = 0, \sigma = 1)$$

therefore dE/dx itself follows log-normal distribution:

$$f(dE/dx) = \mathcal{L}og\mathcal{N}(dE/dx; \mu = \langle dE/dx \rangle, \sigma = \sigma_{dE/dx}) = \frac{1}{\sqrt{2\pi} \cdot \sigma \cdot dE/dx} e^{-\frac{\ln^2 \frac{dE/dx}{\langle dE/dx \rangle}}{2\sigma^2}}$$

The transformation we want to apply should preserve the shape of dE/dx (so that it is still described by  $\mathcal{L}og\mathcal{N}$ ), however it should change  $\mu$  and  $\sigma$  so that these values are eugal to those seen in the data. The transformation that satisfies above postulate is

$$dE/dx' = c \cdot (dE/dx)^a$$

Parameters of the distribution  $\mathcal{L}og\mathcal{N}(dE/dx')$  would be then

$$\mu' = c \cdot \mu^a, \quad \sigma' = a \cdot \sigma$$

From above we get formulae for parameters of the transformation:

$$a = \sigma'/\sigma, \quad c = \frac{\mu'}{\mu^a}$$

AlternativeToCrystallBall [19] Eq. (4.6)

$$f(dE/dx) = \begin{cases} \frac{A}{\sqrt{2\pi} \cdot \sigma \cdot dE/dx} \exp\left(-\frac{1}{2} \left(\frac{\ln \frac{dE/dx}{\langle dE/dx \rangle}}{\sigma}\right)^{2}\right) & \text{for } \frac{\ln \frac{dE/dx}{\langle dE/dx \rangle}}{\sigma} \leq k \\ \frac{A}{\sqrt{2\pi} \cdot \sigma \cdot dE/dx} \exp\left(-k \cdot \frac{\ln \frac{dE/dx}{\langle dE/dx \rangle}}{\sigma} + \frac{1}{2}k^{2} - k^{-1} \left(\frac{\ln \frac{dE/dx}{\langle dE/dx \rangle}}{\sigma} - 1\right)^{k}\right) & \text{for } \frac{\ln \frac{dE/dx}{\langle dE/dx \rangle}}{\sigma} > k \end{cases}$$
(4.6)

$$g(p) = P_1 + P_2 \cdot \exp(-P_3 \cdot p) + P_4 \cdot \arctan(P_5 \cdot (p - P_6))$$
(4.7)

PID	$\langle dE/dx  angle_{ m Bichsel} - \langle dE/dx  angle_{ m MC}$						$\sigma (dE/dx)_{ m MC}$					
1110	$P_1$	$P_2$	$P_3$	$P_4$	$P_5$	$P_6$	$P_1$	$P_2$	$P_3$	$P_4$	$P_5$	$P_6$
$\pi^\pm$	3.618e-8	5.838e-9	5.481				0.0809	-0.023	0.450	-7.84e-3	1.8489	1.04
$K^{\pm}$	-1.01e-10	-9.983e-6	7.581				0.0628	0.022	5.381	3.06e-3	7.3070	0.547
$p,ar{p}$	-4.041e-8	-1.179e-5	4.277				0.0660	0.082	12.042	1.07e-3	7.2872	0.889
$e^\pm$	-1.542e-7	3.393e-7	5.025				0.0572	0.982	37.984	2.61e-3	-27.995	0.693
$\overline{d}, \overline{d}$	-2.469e-6	0.3706	21.654	5.131e-7	30.050	0.781	0.1311	-0.971	4.691			

(a)												
PID	$\langle dE/dx  angle_{ m Bichsel} - \langle dE/dx  angle_{ m Data}$						$\sigma (dE/dx)_{ m Data}$					
	$P_1$	$P_2$	$P_3$	$P_4$	$P_5$	$P_6$	$P_1$	$P_2$	$P_3$	$P_4$	$P_5$	$P_6$
$\pi^{\pm}$	-1.236e-8	1.777e-7	9.938				0.0738	16.86	39.44	-1.704e-3	6.482	0.628
$K^{\pm}$	5.49e-10	-2.732e-6	7.712				0.0743	2.67e-5	7.17089			
$p,ar{p}$	-2.140e-7	0.0421	48.305	7.512e-8	15.544	0.575	0.0779	1.822	22.4277			
$e^{\pm}$	6.701e-8	3.304e-7	7.845				0.0678	468.9	59.4001			
$d, ar{d}$	-1.631e-7	0.0818	18.91				0.1259	-0.288	3.28733			
(b)												

Table 4.1: Parameters of functions from Fig. 4.4 describing track dE/dx as a function of reconstructed momentum for a few particle species. Units of parameters  $P_i$  are such that if one provides momentum in Eq. (4.7) in GeV/c the resultant offset of dE/dx MPV with respect to Bichsel parametrization is in GeV/cm, and the resultant  $\sigma$  parameter is unitless.

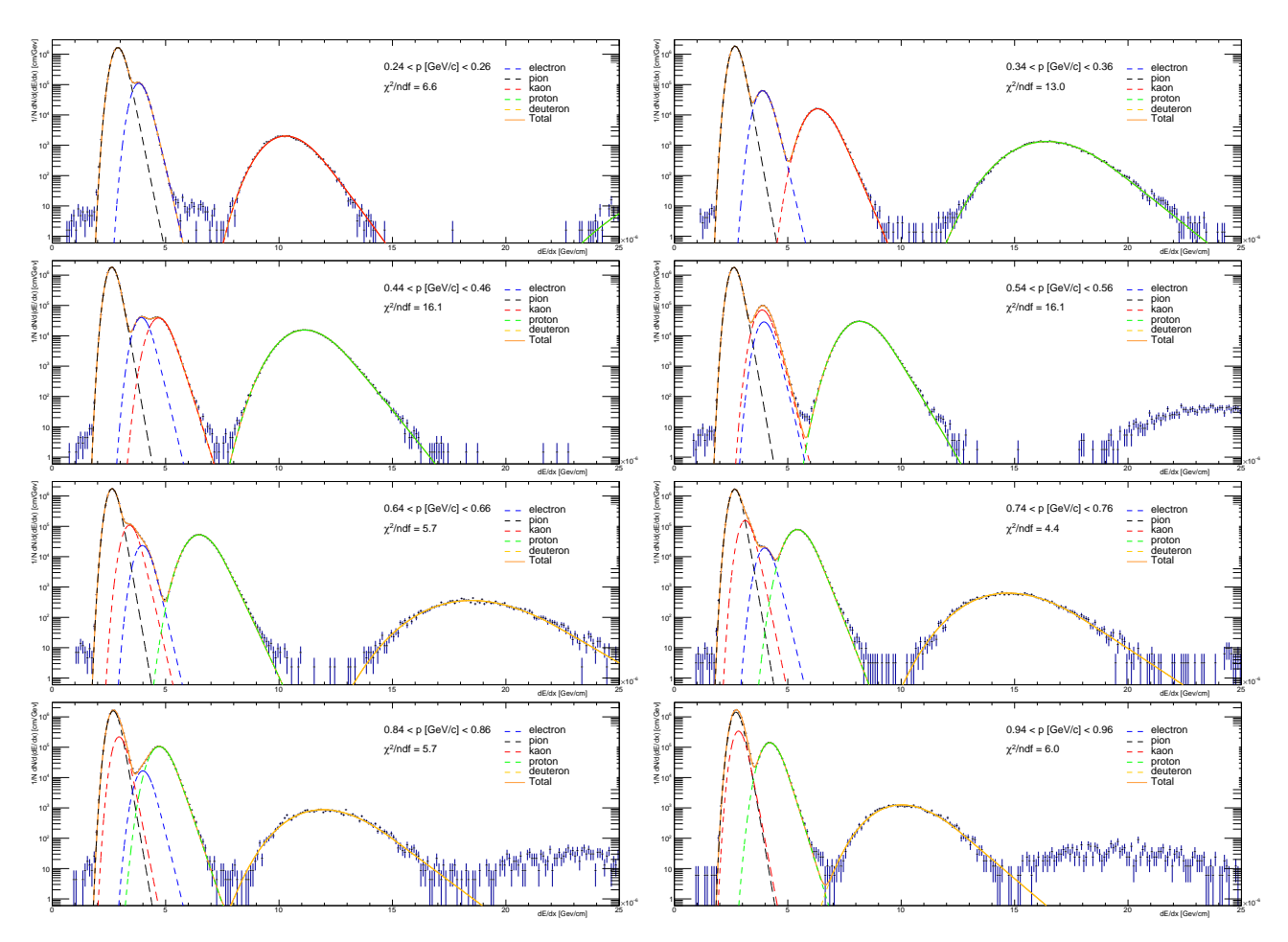


Figure 4.3: Fits of sum of functions from Eq. (4.6) corresponding to different particle species to dE/dx spectra from the data in a few momentum bins.

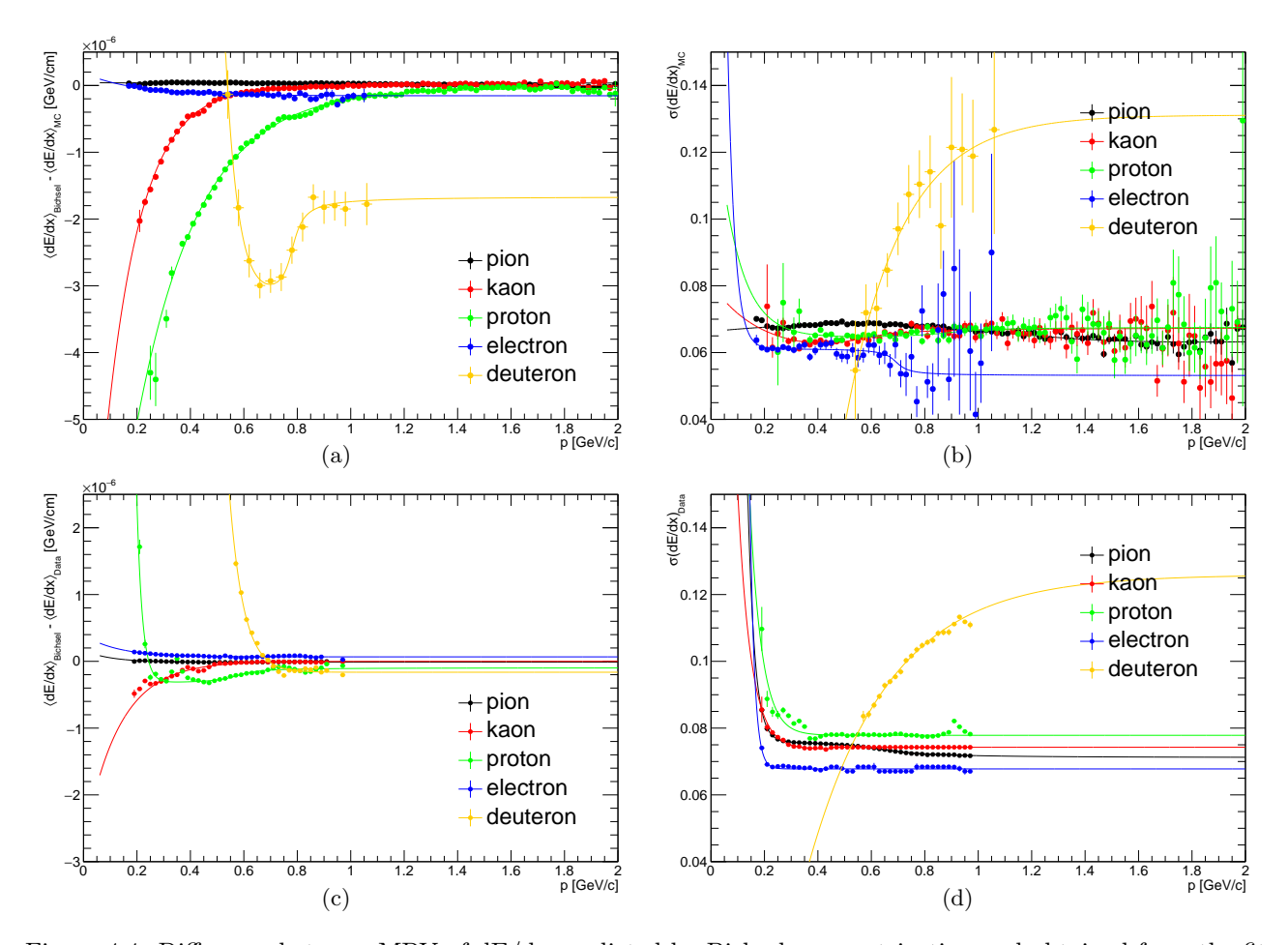


Figure 4.4: Difference between MPV of dE/dx predicted by Bichsel parametrization and obtained from the fit of Eq. (4.6) to dE/dx distribution in the data (4.4c) and MC sample (4.4a) and dE/dx width parameter in data (4.4d) and MC (4.4b) as a function of reconstructed particle momentum for a few particle species. Solid lines represent fits to points of corresponding color.

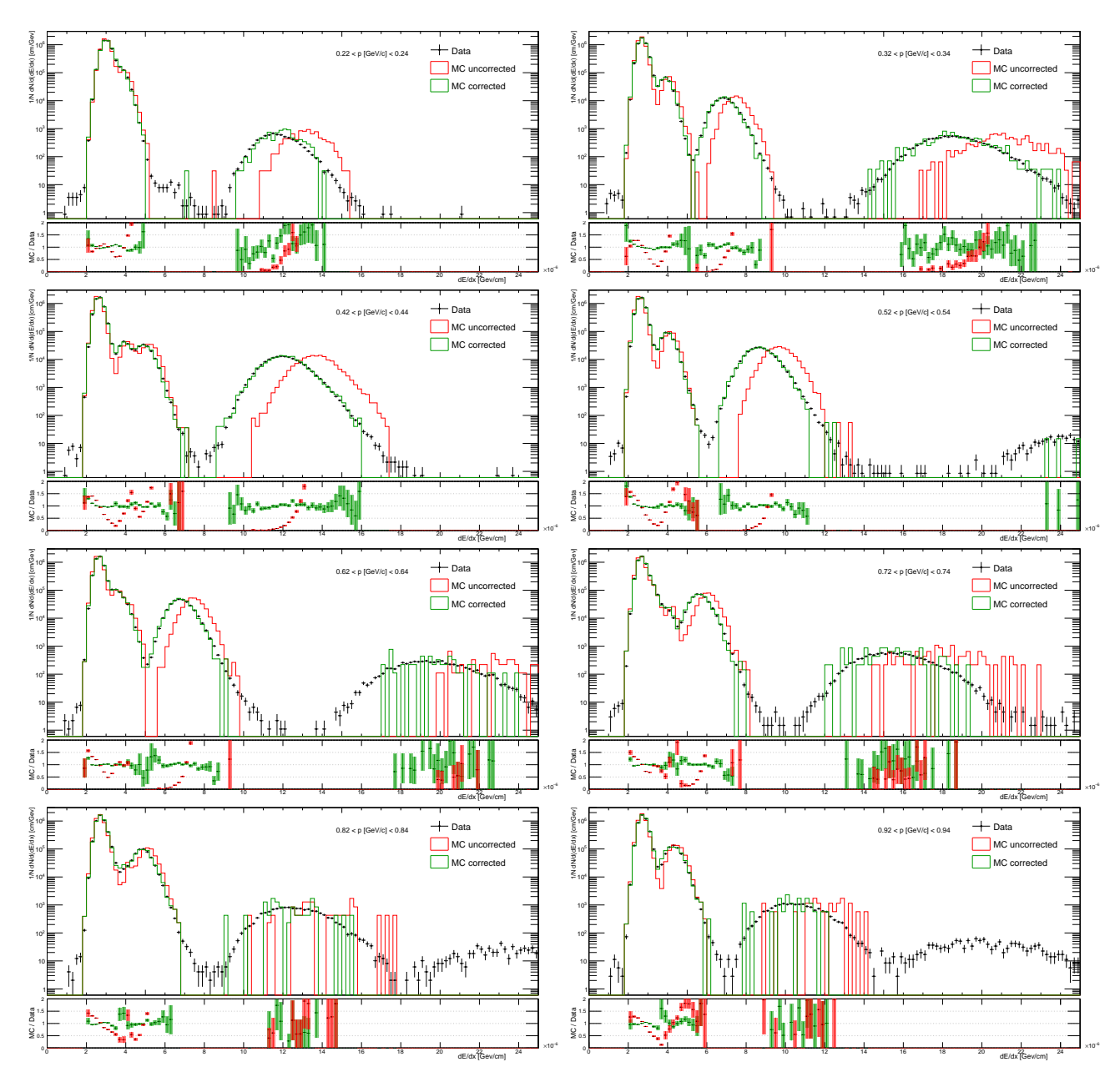


Figure 4.5: Comparison of the dE/dx spectra between the data and MC (before and after correction) in a few momentum bins.

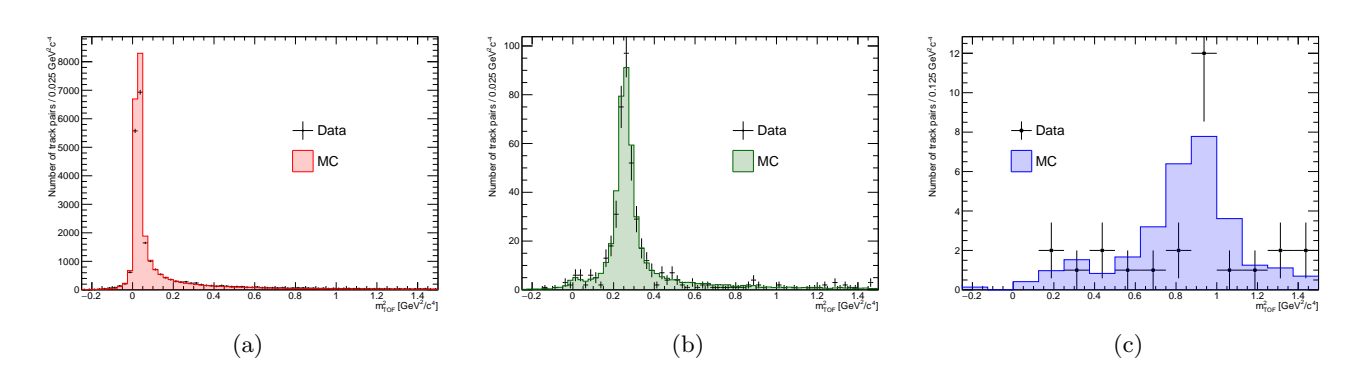


Figure 4.6: Comparison of  $m^2$  from TOF between data and MC for exclusive  $\pi^+\pi^-$ ,  $K^+K^-$  and  $p\bar{p}$ .

### 4.2.3 RP track acceptance and reconstruction efficiency

#### 4.2.4 TPC track acceptance and reconstruction efficiency

We define joint acceptance and efficiency of the reconstruction of a track in the TPC,  $\epsilon_{\text{TPC}}$ , as the probability that particle from the primary interaction generates signal in the detector which is reconstructed as a track that satisfies all quality criteria and whose  $p_T$  and  $\eta$  are within the kinematic region of the measurement (cuts C3.3 and C3.4).

The chnically this quantity is derived from STARsim MC embedded into zero-bias triggers in the following procedure:

- 1. True-level primary particles of given ID and charge, with all physics  $(p_T^{\text{true}}, \eta^{\text{true}})$  and detector  $(z_{\text{vx}})$  quantities within defined region of the measurement, are selected (set A).
- 2. Each particle from set A is checked if global TPC track with more than half of hit points generated by this particle, was reconstructed. All global tracks which are associated with true-level primary particles and satisfy kinematic and quality criteria (cuts C3.3 and C3.4), form set B.
- 3. The joint TPC acceptance and efficiency is calculated as the ratio of the histograms of true-level quantities (such as  $p_T$ ,  $\eta$ ,  $z_{vx}$ ) for particles from set B and particles from set A:

$$\epsilon_{\text{\tiny TPC}}(p_T, \eta, z_{vx}; \text{ sign}, \text{PID}) = \frac{(p_T, \eta, z_{vx}) \text{ histogram for particles of given sign and ID from } set B}{(p_T, \eta, z_{vx}) \text{ histogram for particles of given sign and ID from } set A}.$$
(4.8)

## 4.2.5 TOF acceptance, reconstruction and track-matching efficiency

Combined TOF acceptance, hit reconstruction efficiency and matching efficiency with TPC tracks,  $\epsilon_{\text{TOF}}$ , is defined as the probability that the global TPC track that satisfy kinematic and quality criteria (cuts C3.3 and C3.4) is matched with hit in TOF (matching flag of the track is different from 0). This quantity is generally referred as "TOF efficiency".

It is calculated in two ways. In the first approach the STARsim MC embedded into zero-bias triggers is used. Tracks belonging to  $set\ B$  from Sec. 4.2.4 are utilized. From these tracks a sub-sample of tracks with non-zero TOF matching flag is extracted ( $set\ C$ ). The TOF efficiency is calculated as

$$\epsilon_{\text{TOF}}(p_T, \eta, z_{vx}; \text{ sign}, \text{PID}) = \frac{(p_T, \eta, z_{vx}) \text{ histogram for particles of given sign and ID from } set C}{(p_T, \eta, z_{vx}) \text{ histogram for particles of given sign and ID from } set B}.$$
(4.9)

#### 4.2.6 TPC vertex reconstruction efficiency

The definition of vertex reconstruction efficiency established in this analysis is the probability that two global tracks, both associated with true-level primary particles from the kinematic region of the measurement, both satisfying kinematic and quality criteria (cuts C3.3 and C3.4) and both matched with hits in TOF, form a vertex listed in the collection of reconstructed primary vertices and DCA(R) and DCA(z) of both global tracks calculated w.r.t. this vertex is contained within the limits of cut C3.5.

# 4.3 Particle energy loss

## 4.4 Background subtraction

# 4.5 Unfolding

# 5. Backgrounds

# 5.1 Sources of background

# 5.1.1 Non-exclusive background

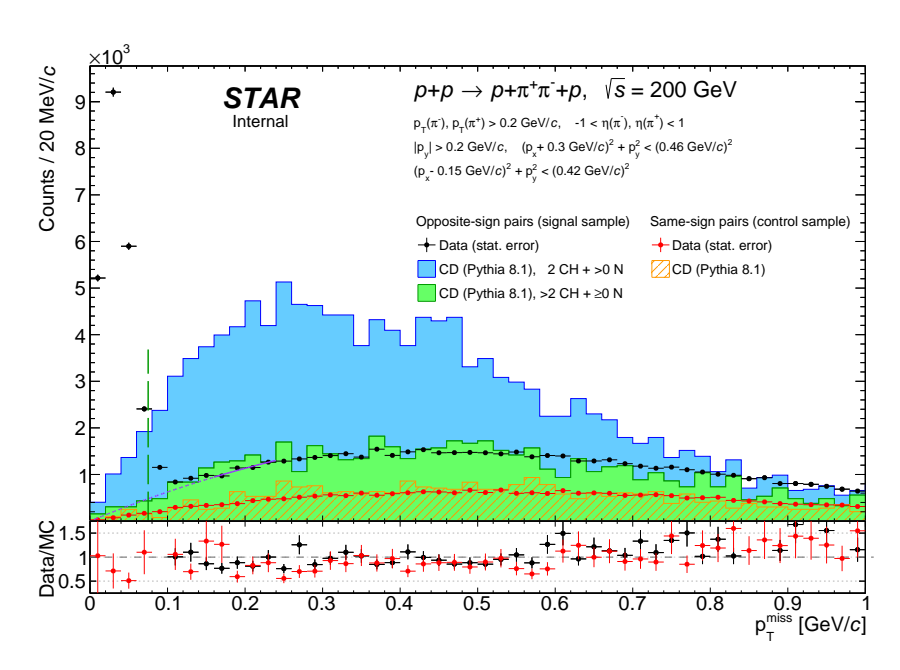


Figure 5.1: Missing pT.

tutaj dodac szkice spodziewanego tla nieekskluzywnego

# 5.1.2 Exclusive background (particle misidentification)

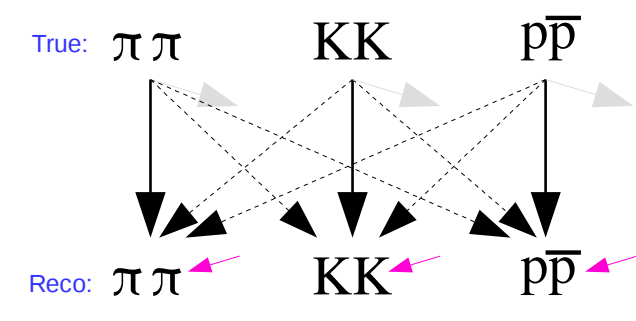


Figure 5.2: Graph illustrating the misidentification problem - the origin of exclusive background in selected samples. Gray arrows represent event rejection due to failed PID selection (C9). Magenta arrows indicate non-exclusive backgrounds described in Sec. 5.1.1. Solid black arrows represent successful identification, whereas dashed black lines show misidentification paths.

$$N_{R}^{\pi\pi} = \underbrace{\epsilon^{\pi\pi} \cdot N_{T}^{\pi\pi}}_{\text{true pion pairs}} + \underbrace{\lambda^{KK \to \pi\pi} \cdot N_{T}^{KK}}_{\text{kaon pairs reconstructed as pion pairs}}_{\text{kaon pairs}} + \underbrace{\lambda^{p\bar{p} \to \pi\pi} \cdot N_{T}^{p\bar{p}}}_{\text{proton pairs reconstructed as pion pairs}} + \underbrace{N_{bkgd}^{\pi\pi}}_{\text{bkgd}}$$
(5.1a)
$$N_{R}^{KK} = \underbrace{\lambda^{\pi\pi \to KK} \cdot N_{T}^{\pi\pi}}_{\text{pion pairs reconstructed as kaon pairs}} + \underbrace{\epsilon^{KK} \cdot N_{T}^{KK}}_{\text{true kaon pairs}} + \underbrace{\lambda^{p\bar{p} \to KK} \cdot N_{T}^{p\bar{p}}}_{\text{proton pairs reconstructed as kaon pairs}} + \underbrace{N_{bkgd}^{KK}}_{\text{bkgd}}$$
(5.1b)
$$N_{R}^{p\bar{p}} = \underbrace{\lambda^{\pi\pi \to p\bar{p}} \cdot N_{T}^{\pi\pi}}_{\text{pion pairs reconstructed}} + \underbrace{\lambda^{KK \to p\bar{p}} \cdot N_{T}^{KK}}_{\text{kaon pairs reconstructed}} + \underbrace{\epsilon^{p\bar{p}} \cdot N_{T}^{p\bar{p}}}_{\text{true proton pairs}} + \underbrace{N_{bkgd}^{p\bar{p}}}_{\text{bkgd}}$$
(5.1c)

Eqs. (5.1) can be written in the matrix form, as shown in Eq. (5.2), from which it is straightforward to obtain final formula for unfolded number of events of given ID, Eq. (5.3):

$$\begin{bmatrix} N_{R}^{\pi\pi} - N_{bkgd}^{\pi\pi} \\ N_{R}^{KK} - N_{bkgd}^{KK} \\ N_{R}^{p\bar{p}} - N_{bkgd}^{p\bar{p}} \end{bmatrix} = \underbrace{\begin{bmatrix} \epsilon^{\pi\pi} & \lambda^{KK \to \pi\pi} & \lambda^{p\bar{p} \to \pi\pi} \\ \lambda^{\pi\pi \to KK} & \epsilon^{KK} & \lambda^{p\bar{p} \to KK} \\ \lambda^{\pi\pi \to p\bar{p}} & \lambda^{KK \to p\bar{p}} & \epsilon^{p\bar{p}} \end{bmatrix}}_{\text{"mixing matrix" } \Lambda} \begin{bmatrix} N_{T}^{\pi\pi} \\ N_{T}^{KK} \\ N_{T}^{p\bar{p}} \end{bmatrix} \rightarrow \begin{bmatrix} N_{T}^{\pi\pi} \\ N_{K}^{KK} \\ N_{T}^{p\bar{p}} \end{bmatrix} = \Lambda^{-1} \begin{bmatrix} N_{R}^{\pi\pi} - N_{bkgd}^{\pi\pi} \\ N_{R}^{KK} - N_{bkgd}^{KK} \\ N_{R}^{p\bar{p}} - N_{bkgd}^{p\bar{p}} \end{bmatrix}$$

$$(5.3)$$

# 5.2 Background and signal normalization

# 6. Systematic errors

# List of Figures

1.1	Central Exclusive Production in $\eta$ - $\phi$ space	4
	•	
2.1	Sketch of the trigger components used in definitions of diffractive triggers in run 15	(
2.2	Beam-detector distance of the Roman Pots in run 15	7
3.1	Primary vertex multiplicty and z-position of the single primary vertex	Ć
3.2	Comparison of distribution of $N_{\rm hits}^{\rm fit}$ , $N_{\rm hits}^{\rm dE/dx}$ and $N_{\rm hits}^{\rm fit}/N_{\rm hits}^{\rm poss}$ in the data and embedded MC	10
3.3	Comparison of distribution of $d_0$ and $z_0$ in the data and embedded MC	11
3.4	Comparison of distribution of $DCA(R)$ and $DCA(z)$ in the data and embedded MC	11
3.5	Comparison of distribution of track $\eta$ and $\phi$ in the data and embedded MC	12
3.6	Local angles of global tracks in Roman Pots.	13
3.7	Correlation and difference of z-vertex position measured in Roman Pots and TPC	13
3.8	Delta z-vx.	14
3.9	MaxAdcBbcLarge	14
3.10	NTofClusters	15
3.11	Correlation between sum of corresponding momentum components ( $x$ in Fig. 3.11a and $y$ in	
	Fig. 3.11b) of Roman Pot proton tracks and TPC tracks	15
3.12	MissingPt	16
3.13	Scheme of two central tracks with common vertex, hitting cells in TOF detector	16
3.14	Correlation between $n\sigma^{\text{pair}}$ from TPC for $\pi^+\pi^-$ , $K^+K^-$ and $p\bar{p}$	17
3.15	Correlation between $m^2$ from TOF and $n\sigma^{\text{pair}}$ from TPC for $\pi^+\pi^-$ , $K^+K^-$ and $p\bar{p}$	17
3.16	Squared particle mass from TOF for candidates of given PID selected based on $dE/dx$ in TPC.	17
3.17	Relation between $\pi^+\pi^-$ significance, efficiency and purity vs. thresholds in cuts C6, C7 and C8.	18
3.18	Cut flow.	19
4.1	Overall efficiency of the online BBC-small and ZDC veto as a function of instantaneous luminosity.	20
4.2	Overall efficiency of the online BBC-small and ZDC veto, primary vertices limit (C1), BBC-large	
	veto (C6) and TOF clusters limit (C7) as a function of instantaneous luminosity	21
4.3	Fits to dE/dx spectra from the data	22
4.4	Parameters of track $dE/dx$ as a function of reconstructed momentum for a few particle species.	23
4.5	Comparison of dE/dx spectra between data and MC	24
4.6	Comparison of $m^2$ from TOF between data and MC for exclusive $\pi^+\pi^-$ , $K^+K^-$ and $p\bar{p}$	24
5.1	Missing pT	26
5.2	Graph illustrating the misidentification problem.	26

# List of Tables

2.1 Central Diffraction physics triggers and control triggers involving Roman Pot detectors in run 15. 6

# References

- P. D. B. Collins, An Introduction to Regge Theory and High-Energy Physics. Cambridge Monographs on Mathematical Physics. Cambridge Univ. Press, Cambridge, UK, 2009. http://www-spires.fnal.gov/spires/find/books/www?cl=QC793.3.R4C695.
- [2] S. Donnachie, H. G. Dosch, O. Nachtmann, and P. Landshoff, Pomeron physics and QCD, vol. 19. 2002.
- [3] V. Barone and E. Predazzi, *High-Energy Particle Diffraction*, vol. v.565 of *Texts and Monographs in Physics*. Springer-Verlag, Berlin Heidelberg, 2002. http://www-spires.fnal.gov/spires/find/books/www?cl=QC794.6.C6B37::2002.
- [4] P. Lebiedowicz and A. Szczurek, "Exclusive  $pp \to pp\pi^+\pi^-$  reaction: From the threshold to LHC," *Phys. Rev.* **D81** (2010) 036003, arXiv:0912.0190 [hep-ph].
- [5] P. Lebiedowicz, O. Nachtmann, and A. Szczurek, "Central exclusive diffractive production of  $\pi^+\pi^-$  continuum, scalar and tensor resonances in pp and  $p\bar{p}$  scattering within tensor pomeron approach," Phys. Rev. **D93** no. 5, (2016) 054015, arXiv:1601.04537 [hep-ph].
- [6] L. A. Harland-Lang, V. A. Khoze, and M. G. Ryskin, "Modelling exclusive meson pair production at hadron colliders," Eur. Phys. J. C74 (2014) 2848, arXiv:1312.4553 [hep-ph].
- [7] R. Fiore, L. Jenkovszky, and R. Schicker, "Resonance production in Pomeron-Pomeron collisions at the LHC," Eur. Phys. J. C76 no. 1, (2016) 38, arXiv:1512.04977 [hep-ph].
- [8] F. E. Close and A. Kirk, "A Glueball q anti-q filter in central hadron production," *Phys. Lett.* **B397** (1997) 333–338, arXiv:hep-ph/9701222 [hep-ph].
- [9] https://online.star.bnl.gov/rp/pp200/.
- [10] https://online.star.bnl.gov/RunLogRun15/.
- [11] http://www.star.bnl.gov/protected/common/common2015/trigger2015/lumipp200GeV/.
- [12] I. Alekseev and J. H. Lee, "Trigger Definitions for RP phase-II\* for Run15." https://drupal.star.bnl.gov/STAR/system/files/trigger\_updated\_run15\_v2.doc, December, 2014.
- [13] I. Alekseev, "Trigger with Roman Pots Phase II\*." https://drupal.star.bnl.gov/STAR/system/files/trigger4RP2\_v2.pdf, December, 2014.
- [14] R. Sikora, "Naming convention and layout of the Roman Pot Phase II\* subsystem in the STAR experiment." https://drupal.star.bnl.gov/STAR/system/files/RomanPotNomenclature\_0.pdf, October, 2014.
- [15] http://www.star.bnl.gov/public/comp/prod/DataSummary.html.
- [16] https://drupal.star.bnl.gov/STAR/event/2017/09/27/software-and-computing-meeting/revertexing-2015-rp-stream.
- [17] L. Adamczyk. https://drupal.star.bnl.gov/STAR/system/files/talk\_42.pdf, March, 2016.
- [18] https://github.com/rafalsikora/CEP-STAR.
- [19] S. Das, "A simple alternative to the Crystal Ball function," arXiv:1603.08591 [hep-ex].